Part I
Nanostructured Devices

Nonlinear Laser Dynamics: From Quantum Dots to Cryptography, First Edition. Edited by Kathy Lüdge.

1
Modeling Quantum-Dot-Based Devices

Kathy Lüdge

1.1
Introduction

During the past decades, the performance of semiconductor lasers has been dramatically improved from a laboratory curiosity to a broadly used light source. Owing to their small size and low costs, they can be found in many commercial applications ranging from their use in DVD players to optical communication networks. The rapid progress in epitaxial growth techniques allows to design complex semiconductor laser devices with nanostructured active regions and, therefore, interesting dynamical properties. Future high-speed data communication applications demand devices that are insensitive to temperature variations and optical feedback effects, and provide features such as high modulation bandwidth and low chirp, as well as error-free operation. Currently, self-organized semiconductor quantum dot (QD) lasers are promising candidates for telecommunication applications [1]. For an introduction to QD-based devices, their growth process, and their optical properties, see, for example, [2, 3].

This review focuses on the modeling of these QD laser devices and on the discussion of their dynamic properties. It uses a microscopically based rate equation model that assumes a classical light field but includes microscopically calculated scattering rates for the collision terms in the carrier rate equations, as introduced in [4–8]. Following the hierarchy of different semiconductor modeling approaches (for an overview, see [9]), this model aims to be sophisticated enough to permit a quantitative modeling of the QD laser dynamics but still allows an analytic treatment of the dynamics. Different levels of complexity will be explored to enable comprehensive insights into the underlying processes.

In order to reduce the numeric effort and still allow for analytic insights, a variety of effects have been neglected. This way, a different approach has to be chosen if, for example, the photon statistics of the emitted light [10] or changes in the emission wavelength due to Coulomb enhancement effects [11, 12] are to be of interest. For the analysis of ultrafast phenomena, as, for example, the gain recovery in QD-based optical amplifiers [13], coherent effects resulting from the dynamics of the microscopic polarization become important, and the model has to be extended

Nonlinear Laser Dynamics: From Quantum Dots to Cryptography, First Edition. Edited by Kathy Lüdge.

to semiconductor Bloch equations. This has been intensively studied in [14, 15] in good agreement with experimental results [16], but it will not be discussed in this review. Note that later on in this book, the experimental results obtained with QD lasers under optical injection are presented in Chapter 3 (by Sciamanna [17]), and the results regarding the sensitivity of QD lasers to optical feedback [18] are discussed in Chapter 6 by Erneux *et al.* [19].

After a detailed introduction to the microscopical modeling aspects in Section 1.2, the turn-on and switching dynamics of a QD laser with two confined levels is discussed in Sections 1.3 and 1.4, and temperature effects are analyzed in Section 3.1. In Section 1.5, the results of an asymptotic analysis of the rate equation systems are presented, which allows to give analytic expression to relaxation oscillation (RO) frequency and damping of the turn-on dynamics, and thus allows to predict the modulation properties of the laser. Resulting from the analytic predictions, the effect of using a doped carrier reservoir on the laser dynamics is investigated in Section 1.6. At the end, in Section 1.7, the results are discussed and compared to quantum well (QW) laser devices.

1.2
Microscopic Coulomb Scattering Rates

A schematic view of the QD laser structure is shown in Figure 1.1a. The active area of the p–n heterojunction is a dot-in-a-well (DWELL) structure that consists of several InGaAs QW layers that have a height of about 4 nm, and contain embedded QDs that are confined in all three dimensions having a size of approximately 4 nm × 18 nm × 18 nm. During laser operation, an electric current is injected into

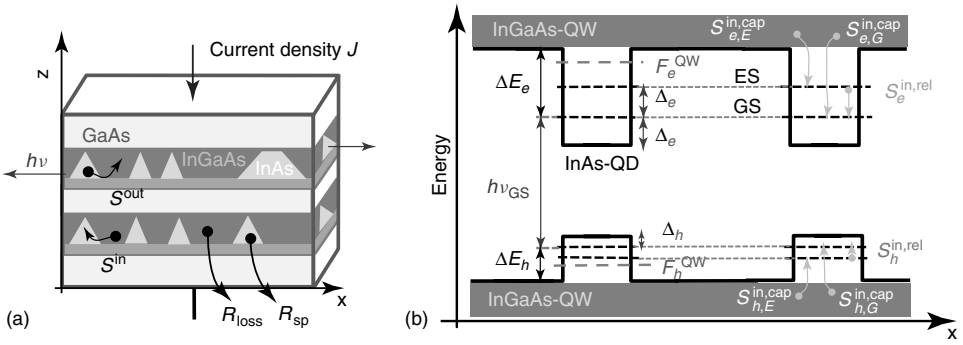

Figure 1.1 (a) Schematic illustration of the QD laser. (b) Energy diagram of the band structure across two QDs in the electron–hole picture. $h\nu_{GS}$ labels the ground state (GS) lasing energy. ΔE_e and ΔE_h mark the distance of the GS from the band edge of the 2D carrier reservoir (QW) for electrons and holes, respectively. Δ_e and Δ_h denote the distance to the bottom of the QD, which is equal to the energetic distances between the GS and the excited state (ES) in the QD. F_e^{QW} and F_h^{QW} are the quasi-Fermi levels for electrons and holes in the QW, respectively. The different processes of direct electron and hole capture ($S^{in,cap}$), as well as relaxation ($S^{in,rel}$) into the QD states, are indicated with gray arrows.

the QW layers. They form the carrier reservoir where carrier–carrier scattering events take place because of Coulomb interaction and lead to a filling (or depletion) of the confined QD levels. As a result, carrier inversion is reached first between the lowest confined QD levels in the conduction band and its counterpart in the valence band. Since the size and the composition of the zero-dimensional QD structures determine the energetic position of the QD levels, it is possible to design lasers with different emission wavelengths. The lasers discussed here have a ground state (GS) emission wavelength of 1.3 μm, as needed for optical data communication.

For high carrier densities in the reservoir, that is, during electrical pumping, the Coulomb interaction (carrier–carrier Auger scattering) will dominate the scattering rate into (and out of) the QDs, whereas the scattering events resulting from carrier–phonon interaction are negligible [20]. Inside the QD, two confined energy levels are modeled. Thus, direct capture processes for electrons ($b = e$) and holes ($b = h$) into or out of the GS labeled as $S^{\text{cap}}_{b,\text{G}}$, into or out of the excited state (ES) labeled as $S^{\text{cap}}_{b,\text{E}}$, and relaxation processes between GSs and ESs named S^{rel}_{b} are considered as depicted in Figure 1.1b, where gray arrows indicate the in-scattering events.

Section 1.2.1 systematically describes and quantifies the different Auger processes before they are incorporated into the dynamic rate equation model in Section 1.3. Note that although phonon scattering between the carrier reservoir (QW) and the QDs is neglected, the fast phonon- assisted carrier relaxation processes within the QW states are taken into account by assuming a quasi-Fermi distribution with quasi-Fermi levels F^{QW}_{e} and F^{QW}_{h} for electrons in the conduction band and holes in the valence band of the QW, respectively.

1.2.1
Carrier–Carrier Scattering

If the Coulomb interaction is treated in the second-order Born approximation in the Markov limit up to second order in the screened Coulomb potential [21, 22], a Boltzmann equation for the collision terms, which describe the change in the occupation probability in the QD states, can be derived, and subsequently easily incorporated into laser rate equation models (for details, see also [15]). The striking difference from the standard rate equation models is that there are no constant relaxation times. Instead, the detailed modeling of the scattering events inside the reservoir leads to scattering times that are nonlinearly dependent on the carrier densities in the reservoir.

Figure 1.2 gives a systematic overview of all processes leading to in-scattering into the QD electron levels. The gray arrows denote electron transitions of the scattering partners. Panels I and III show pure e–e processes, while panels II and IV display mixed e–h processes. The corresponding processes for in-scattering into the QD hole levels are obtained by exchanging all electron and hole states. The out-scattering processes are obtained by inverting all arrows of the electron transitions. The exchange processes of pure e–e capture processes contributing to the scattering rates are not shown, since there is no qualitative difference from that of the direct processes. In case of mixed e–h processes (II, IV), the exchange processes lead to

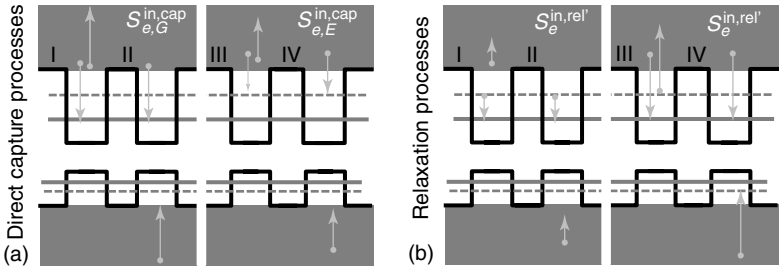

Figure 1.2 Electron transitions during Auger scattering processes (gray arrows denote electron transitions): (a) direct electron capture from the 2D carrier reservoir to the QD ground state (I, II) and first excited state (III, IV). Panels I and III and panels II and IV show pure e–e and mixed e–h scattering processes, respectively. (b) QW-assisted intradot electron relaxation to the QD ground state.

transitions across the band gap, which are neglected since they are unlikely to occur. Note that the process shown in panel III of Figure 1.2b is the exchange process of the one in panel I. In the following, the scattering events shown in Figure 1.2 are decomposed into contributions originating from direct carrier capture from the QW into the QD levels R_m^{cap} (Figure 1.2a) and relaxation processes between the QD states with one and two intra-QD transitions $R^{rel'}$ and $R^{rel''}$, respectively (Figure 1.2b). Processes involving three QD states are neglected. Thus, the collision term in the Boltzmann equation for the carrier occupation probability in the QD states ρ_b^m, where m labels the quantum number of the 2D angular momentum of the confined QD states ($m = \mathrm{E}$ for the first ES; $m = \mathrm{G}$ for the GS) reads:

$$\frac{\partial \rho_b^m}{\partial t}|_{col} = R_{b,m}^{cap} + R_b^{rel'} + R_b^{rel''} \tag{1.1}$$

The contribution to Eq. (1.1) from direct capture processes (Figure 1.2a) can be expressed as

$$R_{b,m}^{cap} = S_{b,m}^{in,cap}(1 - \rho_b^m) - S_{b,m}^{out,cap}\rho_b^m \tag{1.2}$$

where the direct capture Coulomb scattering rates for in- $\left(S_{b,m}^{in,cap}\right)$ and out-scattering $\left(S_{b,m}^{out,cap}\right)$ are defined as

$$S_{b,m}^{in,cap} = \sum_{k_1 k_2 k_3, b'} W^b_{k_1^b k_3^{b'} k_2^{b'} m} f_{k_1^b} f_{k_3^{b'}} \left(1 - f_{k_2^{b'}}\right) \qquad (k_1 \to m,\ k_3 \to k_2), \tag{1.3}$$

$$S_{b,m}^{out,cap} = \sum_{k_1 k_2 k_3, b'} W^b_{m k_2^{b'} k_3^{b'} k_1^b} \left(1 - f_{k_1^b}\right)\left(1 - f_{k_3^{b'}}\right) f_{k_2^{b'}} \qquad (m \to k_1,\ k_2 \to k_3). \tag{1.4}$$

States in the QW are labeled by the in-plane carrier momentum k_i^b ($b = e$ and $b = h$ indicate conduction and valence band states, respectively). For both bands in the QW, $f_{k_i^b}$ indicates the electron occupation probability. The transition probability $W^b_{k_1 k_2 k_3 m'}$ for a process where two carriers scatter from initial states k_1 and k_3 to the final states m and k_2, respectively, ($k_1 \to m$, $k_3 \to k_2$) contains the

screened Coulomb matrix elements for direct and exchange interactions, and the energy-conserving δ-function [6, 15]. Owing to the microscopic reversibility of the Coulomb matrix elements, the transition probability is equal for reversed direction $W^b_{k_1^b k_3^{b'} k_2^{b'} m} = W^b_{m k_2^{b'} k_3^{b'} k_1^b}$.

The relaxation processes shown in Figure 1.2b describe a redistribution of carriers within the intra-QD levels. The contribution from processes I and II to Eq. (1.1) is given by

$$R_b^{\mathrm{rel}'} = S_b^{\mathrm{in,rel}'} \rho_b^{\mathrm{E}} (1 - \rho_b^{\mathrm{G}}) - S_b^{\mathrm{out,rel}'} (1 - \rho_b^{\mathrm{E}}) \rho_b^{\mathrm{G}}. \tag{1.5}$$

The relaxation in-scattering rate is given by

$$S_b^{\mathrm{in,rel}'} = \sum_{k_2 k_3, b'} W^b_{\mathrm{E}\, k_3^{b'} k_2^{b'}\, \mathrm{G}} \left(1 - f_{k_2^{b'}}\right) f_{k_3^{b'}} \qquad (\mathrm{E}\to\mathrm{G},\ k_3 \to k_2). \tag{1.6}$$

The dynamical equations for the processes III and IV ($R^{\mathrm{rel}''}$) in Figure 1.2b can be obtained in a similar manner as in Eq. (1.5).

For the calculation of the Coulomb scattering rates, a quasiequilibrium *within* the QW states (fast phonon scattering inside one band) but nonequilibrium *between* the QW electrons and the QD electrons, the QW holes, and the QD holes is assumed. As a result, the electron occupation probability f_{k^b} in the conduction ($b = e$) and valence band ($b = h$) of the QW can be expressed by a quasi-Fermi distribution given by

$$f_{k^b} = \left[\exp\left(\frac{E_k - F_b^{\mathrm{QW}}}{kT} \right) + 1 \right]^{-1} \qquad (b = e, h). \tag{1.7}$$

The quasi-Fermi levels F_b^{QW} are determined by the total carrier density in the respective band via the relation given in Eq. (1.8), as shown in [7, 23],

$$F_b^{\mathrm{QW}}(w_b) = E_b^{\mathrm{QW}} \pm kT \ln\left[\exp\left(\frac{w_b}{D_b kT} \right) - 1 \right] \tag{1.8}$$

where the $+$ and $-$ signs correspond to electrons and holes, respectively. Furthermore, $D_b = m_b/(\pi\hbar^2)$ is the 2D density of states, with the effective masses m_b of electrons ($b = e$) and holes ($b = h$), respectively. E_b^{QW} are the QW band edges of conduction and the valence band, respectively. Note that the analytic expression Eq. (1.8) is only valid for a 2D electron gas, where the integrals

$$w_e = \int_{E_e^{\mathrm{QW}}}^{\infty} dE_k D_e f_{k^e} \qquad \text{and} \qquad w_h = \int_{-\infty}^{E_h^{\mathrm{QW}}} dE_k D_h (1 - f_{k^h}) \tag{1.9}$$

can be solved. As a result, the quasi-Fermi distributions f_{k^e} and f_{k^h} are determined by the QW carrier densities w_e and w_h, and thus, the scattering rates given in Eqs. (1.3) and (1.6) are calculated as functions of w_e and w_h. Besides that, the scattering rates parametrically depend on the effective masses of the carriers in the QW bands and on the band structure given by the energetic distances ΔE_b and Δ_b, as indicated in Figure 1.1b. The resulting rates are shown in Figure 1.3 as a function of w_e along the line $w_h/w_e = 1.5$. For the relaxation rates, the sum of all relaxation processes

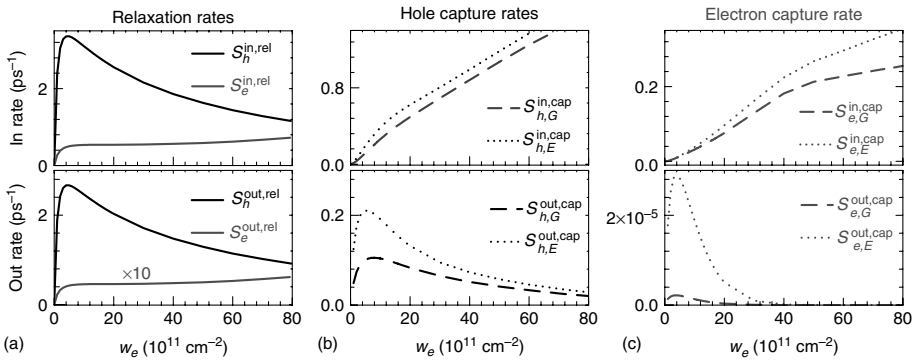

Figure 1.3 Coulomb scattering rates of the QDs-in-a-well system versus QW electron density w_e ($w_h/w_e = 1.5$). (a) Intra-QD relaxation rates for electrons (gray) and holes (black); (b) and (c) direct capture rates into the GS (dashed line) and ES (dotted line) for holes and electrons, respectively. Top and bottom panels show in- and out-scattering rates, respectively. Parameters as in Table 1.1.

is plotted but note that the rates involving a transition within the QD accompanied by a QW transition (rel′) are much larger than the rates involving two QW–QD transitions (rel″). The relaxation rates are characterized first by a sharp increase and later by a decrease in higher carrier densities because of the effect of Pauli blocking. These relaxation scattering events are on a ps time scale, whereas the direct capture rates plotted in Figure 1.3b,c for holes and electrons are an order of magnitude smaller for small carrier densities. Owing to their small effective mass, the rate for electron capture is much smaller, although the dependence on w_e is similar to that of the hole rate. For small electron densities inside the QW, the capture rates increase quadratically with w_e, which is expected from mass action kinetics.

1.2.2 Detailed Balance

In thermodynamic equilibrium, there is a detailed balance between the in- and out-scattering rates of the QD level. This allows one to relate the rate coefficients of in- and out-scattering even for nonequilibrium carrier densities [24].

For a single scattering process between two carriers of type b and b', the in-scattering rate for capture into the GS ($m = \mathrm{G}$) or ES ($m = \mathrm{E}$) is defined in Eq. (1.3), and can be rewritten as

$$W^b_{k_1^b k_3^{b'} k_2^{b'} m} f_{k_1^b} f_{k_3^{b'}} (1 - f_{k_2^{b'}}) \tag{1.10}$$

$$= W^b_{k_1^b k_3^{b'} k_2^{b'} m} (1 - f_{k_1^b})(1 - f_{k_3^{b'}}) f_{k_2^{b'}} \frac{f_{k_1^b}}{1 - f_{k_1^b}} \frac{f_{k_3^{b'}}}{1 - f_{k_3^{b'}}} \frac{1 - f_{k_2^{b'}}}{f_{k_2^{b'}}} \tag{1.11}$$

$$= W^b_{k_1^b k_3^{b'} k_2^{b'} m} (1 - f_{k_1^b})(1 - f_{k_3^{b'}}) f_{k_2^{b'}} \exp\left[\frac{F_e^{\mathrm{QW}} - E_{k_1^b} - E_{k_3^{b'}} + E_{k_2^{b'}}}{kT}\right] \tag{1.12}$$

if the quasi-Fermi distribution given in Eq. (1.7) is used, which leads to $f_k/(1-f_k) = \exp\left[(F_e^{\mathrm{QW}} - E_k)/(kT)\right]$. Inserting the energy conservation of final and initial states, $E_{k_2^{b'}} - E_{k_3^{b'}} - E_{k_1^{b}} + E_{b,m}^{\mathrm{QD}} = 0$, where $E_{b,m}^{\mathrm{QD}}$ is the confined QD energy ($m = \mathrm{G}, \mathrm{E}$) for electrons ($b = e$) or holes ($b = h$), and summing overall initial and final states in k-space gives

$$S_{b,m}^{\mathrm{in,cap}} = S_{b,m}^{\mathrm{out,cap}} e^{\frac{\pm\left(F_b^{\mathrm{QW}} - E_{b,m}^{\mathrm{QD}}\right)}{kT}} = S_{b,m}^{\mathrm{out,cap}} e^{\frac{\Delta E_{b,m}}{kT}} \left[e^{\frac{w_b}{D_b kT}} - 1 \right] \tag{1.13}$$

where $\Delta E_{b,\mathrm{G}} = \pm(E_b^{\mathrm{QW}} - E_{b,\mathrm{G}}^{\mathrm{QD}})$ and $\Delta E_{b,\mathrm{E}} = \pm(E_b^{\mathrm{QW}} - E_{b,\mathrm{E}}^{\mathrm{QD}})$ are the energetic distances from the QW band edge to the GS and the ES of the QD, respectively, and the $+$ and $-$ signs correspond to electrons and holes, respectively.

Note that Eq. (1.13) holds for the mixed e–h Auger capture process ($b \neq b'$) as well as for the e–e and h–h processes. Thus, besides the Boltzmann factor $e^{\frac{\Delta E}{kT}}$ that is valid for a discrete two-level system with energy difference ΔE, the ratio $(S_b^{\mathrm{in}}/S_b^{\mathrm{out}})$ for Auger scattering between the 2D electron gas of the QW and the discrete QD level also depends on the quasi-Fermi levels F_b^{QW}, and thereby on the carrier density in the QW. As a result of this carrier-density-dependent factor in the detailed balance relation, the out-scattering rates show a pronounced maximum around the degeneracy concentration $D_b kT$, as can be seen in the bottom panel of Figure 1.3b,c.

In contrast to that, the ratio between the in- and out-scattering relaxation rates is a constant factor since both involved levels are indeed localized. For the positively defined energy difference Δ_b ($b = e, h$) between ES and GS (Figure 1.1b), the relation reads:

$$S_b^{\mathrm{in,rel}} = S_b^{\mathrm{out,rel}} e^{\frac{\Delta_b}{kT}} \tag{1.14}$$

1.3 Laser Model with Ground and Excited States in the QDs

Using the microscopic scattering rates defined in the last section, an eight-variable rate equation system can be formulated, which contains the Boltzmann collision terms for the direct capture processes, $R_{b,m}^{\mathrm{cap}}$, defined in Eq. (1.2), and those for relaxation into the GS, R_b^{rel}, defined in Eq. (1.5). As used earlier for the scattering contributions in Section 1.2, carrier densities in the GS and ES have the index G and E, respectively, and the index b labels the carrier type. Further, the photon densities $n_{\mathrm{ph}}^{\mathrm{G}}$ and $n_{\mathrm{ph}}^{\mathrm{E}}$ are introduced, which result from the GS and ES transition in the QD, respectively. Starting from the occupation probability of the confined QD levels $\rho_b^{\mathrm{G,E}}$, the carrier densities in the QD are defined by $n_b^{\mathrm{G,E}} = N^{\mathrm{QD}} \nu_{\mathrm{G,E}} \rho_b^{\mathrm{G,E}}$. N^{QD} denotes twice the QD density of the lasing subgroup (the factor of 2 accounts for spin degeneracy), and $\nu_{\mathrm{G,E}}$ is the degeneracy of the states ($\nu_{\mathrm{G}} = 1, \nu_{\mathrm{E}} = 2$).

The induced processes of absorption and emission at the GS wavelength are modeled by a linear gain $R_{\mathrm{ind}}^{\mathrm{G}} = WA(n_e^{\mathrm{G}} + n_h^{\mathrm{G}} - N^{\mathrm{QD}})\, n_{\mathrm{ph}}^{\mathrm{G}}$, where W is the Einstein coefficient that can be determined from a full quantum mechanical approach of the light matter interaction [9], and A is the in-plane area of the QW. Analogous to the simple two-level system, the model introduced above yields positive gains if the occupation probability of electrons in the localized conduction band level $f_e^C = \rho_e^{\mathrm{G}} = n_e^{\mathrm{G}}/N^{\mathrm{QD}}$ of the QDs is higher than the occupation probability of electrons in their localized valence band level $f_e^V = 1 - \rho_h^{\mathrm{G}}$. Thus, the linear gain term $R_{\mathrm{ind}} = WAN^{\mathrm{QD}}(f_e^C - f_e^V)\, n_{\mathrm{ph}} = WAN^{\mathrm{QD}}(f_e^C(1 - f_e^V) - f_e^V(1 - f_e^C))\, n_{\mathrm{ph}}$ corresponds to the standard net rate of stimulated emission minus absorption [25]. The rate of induced emission at the ES wavelength is obtained analogously, but by assuming a different Einstein coefficient $\overline{W}$; thus, $R_{\mathrm{ind}}^{\mathrm{E}} = \overline{W}A(n_e^{\mathrm{E}} + n_h^{\mathrm{E}} - 2N^{\mathrm{QD}})\, n_{\mathrm{ph}}^{\mathrm{E}}$. As a result of the size distribution and material composition fluctuations of the QDs, only a subgroup (QD density N^{QD}) of all QDs (N^{sum}) matches the mode energies for lasing. The QD density N^{sum} is twice the total QD density as given by experimental surface imaging (again, the factor of 2 accounts for spin degeneracy). As discussed below, N^{QD} is not a constant but can increase with increasing pump current if the number of longitudinal modes in the laser output is increased (see Figure 1.9a for experimental lasing spectra).

The nonlinear rate equations (Eqs. (1.15)–(1.19)) describe the dynamics of the charge carrier densities in the GS and ES of the QDs, n_b^{G} and n_b^{E}, respectively, the carrier densities in the QW, w_b, and the photon density emitted from the GS and the ES, $n_{\mathrm{ph}}^{\mathrm{G}}$ and $n_{\mathrm{ph}}^{\mathrm{E}}$, respectively.

$$\dot{n}_b^{\mathrm{E}} = N^{\mathrm{QD}}(2R_{b,\mathrm{E}}^{\mathrm{cap}} - R_b^{\mathrm{rel}}) - \overline{W}A(n_e^{\mathrm{E}} + n_h^{\mathrm{E}} - 2N^{\mathrm{QD}})n_{\mathrm{ph}}^{\mathrm{E}} - \overline{W}n_e^{\mathrm{E}}\rho_h^{\mathrm{E}}, \tag{1.15}$$

$$\dot{n}_b^{\mathrm{G}} = N^{\mathrm{QD}}(R_{b,\mathrm{G}}^{\mathrm{cap}} + R_b^{\mathrm{rel}}) - WA(n_e^{\mathrm{G}} + n_h^{\mathrm{G}} - N^{\mathrm{QD}})n_{\mathrm{ph}}^{\mathrm{G}} - Wn_e^{\mathrm{G}}\rho_h^{\mathrm{G}} \tag{1.16}$$

$$\dot{w}_b = \eta\frac{J(t)}{e_0} - N^{\mathrm{sum}}\left[R_{b,\mathrm{G}}^{\mathrm{cap}} + 2R_{b,\mathrm{E}}^{\mathrm{cap}}\right] - Bw_e w_h, \tag{1.17}$$

$$\dot{n}_{\mathrm{ph}}^{\mathrm{G}} = -2\kappa n_{\mathrm{ph}}^{\mathrm{G}} + \Gamma WA(n_e^{\mathrm{G}} + n_h^{\mathrm{G}} - N^{\mathrm{QD}})n_{\mathrm{ph}}^{\mathrm{G}} + \beta Wn_e^{\mathrm{G}}\rho_h^{\mathrm{G}} \tag{1.18}$$

$$\dot{n}_{\mathrm{ph}}^{\mathrm{E}} = -2\kappa n_{\mathrm{ph}}^{\mathrm{E}} + \Gamma\overline{W}A(n_e^{\mathrm{E}} + n_h^{\mathrm{E}} - 2N^{\mathrm{QD}})n_{\mathrm{ph}}^{\mathrm{E}} + \beta\overline{W}n_e^{\mathrm{E}}\rho_h^{\mathrm{E}} \tag{1.19}$$

The spontaneous emission in each level of the QDs is approximated by bimolecular recombination using $R_{\mathrm{sp}}^{\mathrm{G}}(n_e^{\mathrm{G}}, n_h^{\mathrm{G}}) = Wn_e^{\mathrm{G}}n_h^{\mathrm{G}}/N^{\mathrm{QD}}$ and $R_{\mathrm{sp}}^{\mathrm{E}}(n_e^{\mathrm{E}}, n_h^{\mathrm{E}}) = \overline{W}n_e^{\mathrm{E}}n_h^{\mathrm{E}}/(2N^{\mathrm{QD}})$. The loss rate $R_{\mathrm{loss}}^b = Bw_e w_h$, accounting for carrier losses in the QW, is a sum of the spontaneous band–band recombination and Auger-related losses inside the QW [26]. This loss rate determines the lifetime τ_w^b of carriers in the QW ($R_{\mathrm{loss}}^b \equiv w_b/\tau_w^b$), which is on the order of several nanoseconds and decreases with the carrier densities w_b. β is the spontaneous emission coefficient, and $\Gamma = \Gamma_g N^{\mathrm{QD}}/N^{\mathrm{sum}}$ is the optical confinement factor. Γ is the product of the geometric confinement factor Γ_g (i.e., the ratio of the volume of all QDs and the mode volume), and the ratio $N^{\mathrm{QD}}/N^{\mathrm{sum}}$ (accounting for reduced gain since only a subgroup of all QDs matches the mode energy for lasing because of the size distribution and material composition fluctuations of the QDs). The coefficient $2\kappa = (c/\sqrt{\varepsilon_{\mathrm{bg}}})[\kappa_{\mathrm{int}} - \ln(R_1R_2)/2L]$ expresses the total cavity loss [2], where L is the cavity length, and R_1 and R_2 are the facet reflectivities, and κ_{int} are the

internal losses [6]. J is the injection current density, e_o is the elementary charge, and $\eta = 1 - w_e/N^{\mathrm{QW}}$ is the current injection efficiency that accounts for the fact that the injection into the QW is blocked if the QW is already filled (maximum density inside the QW: $w_e = N^{\mathrm{QW}}$). Note that within the model the carriers are directly injected into the QW, leading, of course, to an underestimation of the experimentally realized current densities. Therefore, only current densities relative to the threshold value J_{th} are considered for comparisons between theory and experiment. The values of parameters used for the simulations are listed in Table 1.1, if not stated otherwise.

The steady-state characteristics and the turn-on dynamics for the QD laser as resulting from the nonlinear rate equations (Eqs. (1.15)–(1.19)) are depicted in Figure 1.4. The input–output curves in Figure 1.4b show that with increasing pump current, the GS first reaches inversion and starts lasing at the GS threshold current $J_{\mathrm{th}}^{\mathrm{G}}$. By further increasing the pump current, the ES reaches its lasing threshold $J_{\mathrm{th}}^{\mathrm{E}}$ and the laser emits light at both wavelengths. As can be seen in Figure 1.4b, the GS efficiency is reduced as soon as the ES lasing sets in. The turn-on dynamics observed before reaching the steady states is shown in Figure 1.4a,c. For currents above $J_{\mathrm{th}}^{\mathrm{G}}$ but far below $J_{\mathrm{th}}^{\mathrm{E}}$, highly damped ROs are found for the GS turn-on trajectories (Figure 1.4a) in accordance with experimental results [26]. Above $J_{\mathrm{th}}^{\mathrm{E}}$, the ES turns on with very short turn-on delay times and damped ROs (gray line in Figure 1.4c), while the GS shows overdamped turn-on behavior (black line in Figure 1.4c). The overdamped behavior is due to the high current needed to invert the ES levels, which is accompanied by high carrier densities in the reservoir and thus by high scattering rates into the GS (see Section 1.5 for analytic discussions of the damping rate, which depends on the carrier lifetimes).

The ratio of the threshold currents of the two modes, $J_{\mathrm{th}}^{\mathrm{E}}/J_{\mathrm{th}}^{\mathrm{G}}$, depends on the values of the carrier capture and relaxation rates and can be changed by varying the band structure of the QD–QW system. A system where the QW band edge is very close to the ES leads to a faster filling of the ES and thus to a smaller $J_{\mathrm{th}}^{\mathrm{E}}$ (compare Figure 1.4b and Figure 1.6c that show the input–output curves for different confinement energies). Besides this microscopic effects, the ratio $J_{\mathrm{th}}^{\mathrm{E}}/J_{\mathrm{th}}^{\mathrm{G}}$ also depends on the device length. Length-dependent measurements of this ratio

Table 1.1 Numerical parameters used in the simulation, unless stated otherwise.

Symbol	Value	Symbol	Value	Symbol	Value
W	$0.7\ \mathrm{ns}^{-1}$	A	$4 \times 10^{-5}\mathrm{cm}^2$	ΔE_e	210 meV
$\overline{W}$	$0.88\ \mathrm{ns}^{-1}$	N^{QD}	$0.6 \times 10^{10}\mathrm{cm}^{-2}$	ΔE_h	50 meV
B	$0.5\ \mathrm{nm}^2\ \mathrm{ps}^{-1}$	N^{sum}	$6 \times 10^{10}\mathrm{cm}^{-2}$	Δ_e	64 meV
Γ_g	0.06	N^{QW}	$1 \times 10^{12}\mathrm{cm}^{-2}$	Δ_h	6 meV
2κ	$0.16\ \mathrm{ps}^{-1}$	β	5×10^{-6}	$D_{e/h}$	$m_{e/h}/(\pi\hbar^2)$
R_1, R_2	0.32	L	1 mm	m_e	$0.043\ m_0$
ε_{bg}	14.2	κ_{int}	$650\ \mathrm{m}^{-1}$	m_h	$0.45\ m_0$

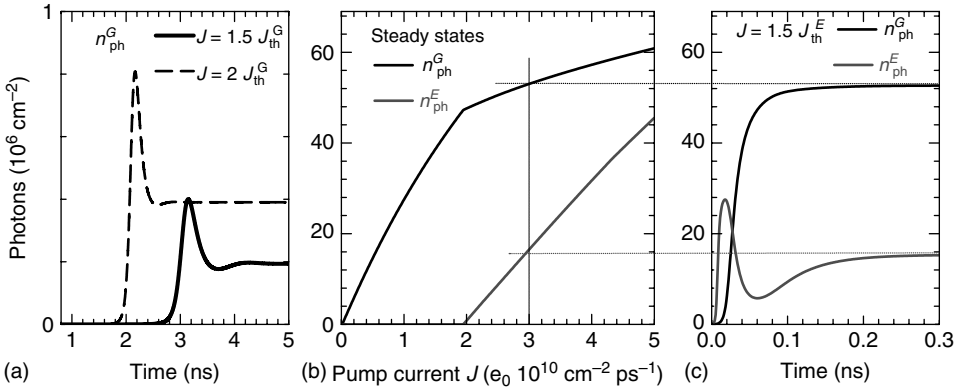

Figure 1.4 Simulated laser turn-on dynamics at the (a) GS lasing wavelength for two different small currents below the ES threshold J_{th}^E and (c) ES and GS lasing above J_{th}^E at $J = 1.5 J_{th}^E$; (b) steady-state photon output from the ES (gray) and GS (black) transition. $J_{th}^E = 1.95 \times 10^8 e_0$ cm^{-2} ps^{-1}; $J_{th}^G = 1.5 \times 10^{10} e_0$ cm^{-2} ps^{-1}. Parameters as in Table 1.1 but $\Delta E_e = 134$ meV, $\Delta E_h = 30$ meV and $B = 0.2$ nm^2 ps^{-1}.

can be found in [27], showing that the shorter the device the smaller is J_{th}^E, while J_{th}^G increases. This is in good agreement with our simulations.

The threshold current J_{th}^G can be obtained from Eqs. (1.15)–(1.19) by deriving the steady-state characteristics of the laser. By neglecting spontaneous emission and photons from the ES transition ($\beta = 0$; $n_{ph}^E = 0$), this leads to

$$n_{ph}^{G\,*}(J) = J_{th}^G \frac{\Gamma N^{QD}}{2\kappa N^{sum}} \left(\frac{J}{J_{th}^G} - 1 \right) \tag{1.20}$$

$$J_{th}^G = B w_{e|th} w_{h|th} + \frac{N^{sum}}{(N^{QD})^2} \left(W n_{e|th}^G n_{h|th}^G + \overline{W} n_{e|th}^E n_{h|th}^E \right). \tag{1.21}$$

Eq. (1.21) shows that J_{th}^G depends upon the loss terms in the rate equations. Thus, the parameters B, W, and N^{sum}, as well as the carrier densities at threshold, labeled with the subscript $|_{th}$ in Eq. (1.21), determine J_{th}^G. The threshold carrier densities are determined by the different scattering contributions (they do not depend on B and N^{sum}). However, owing to the nonlinear dependence of the Auger scattering rates upon the QW carrier densities, it is not possible to give closed analytic expression (see [7] for approximations). The ES threshold current J_{th}^E also depends on the photon density in the GS, which depends on the pump current and the differential gain. The analytic expression reads:

$$J_{th}^E = J_{th}^G + \frac{2\kappa N^{sum}}{\Gamma N^{QD}} n_{ph}^G. \tag{1.22}$$

Since the microscopic model allows for a separate treatment of electron and hole dynamics, the transient behavior of both species will be investigated. Figure 1.5a,b shows the trajectories of the turn-on process projected onto the (n_b^G, n_{ph}^G)-planes. The familiar anticlockwise rotation can be seen for the electron as well as for the

hole density. Nonetheless, their shape is different. The black stars in Figure 1.5a,b denote the steady state values of the electron and hole concentration in the GS levels, n_e^{G*} and n_h^{G*}, respectively, for increasing pump currents. It is interesting to note that the value of n_e^{G*} decreases with J. This is anomalous because the carrier concentration for conventional lasers is clamped at the threshold value (saturation of inversion). Nevertheless, the inversion of the QDs is saturated as the total number of carriers, namely, the threshold density $n_t^G = n_e^{G*} + n_h^{G*}$, is a constant that depends only on the material parameters and not on the pump current. n_t^G can be obtained by neglecting spontaneous emission in Eq. (1.18) and setting $\dot{n}_{ph}^G = 0$:

$$n_t^G = n_e^{G*} + n_h^{G*} = \frac{2\kappa}{\Gamma W A} + N^{QD}. \tag{1.23}$$

Figure 1.5 also reveals that the steady-state values of n_e^{G*} and n_h^{G*} differ a lot. While in the steady state most of the QDs are occupied by an electron, only every fifth hole state is filled. This effect is due to the high out-scattering rates for the holes, which inhibits effective filling of the states. As known from the microscopic scattering rates plotted in Figure 1.3, the hole out-scattering rate decreases with the carrier density in the reservoir and thus with the pump current. This leads to higher n_h^{G*} for higher currents (see [7] for detailed steady-state analysis of a QD laser with one confined level).

As can be seen in the phase portrait of Figure 1.5c, the turn-on process projected onto the (n_e, n_h)-plane deviates from a straight line (which corresponds to the synchronized behavior $n_e \sim n_h$) and instead performs a spiral ending in the fixed point (steady state). This desynchronization between electron and hole dynamics is due to the different carrier lifetimes that stem from the different effective masses and the resulting different energy separation between QW band edge and confined QD level (ΔE_e and ΔE_h in Figure 1.1b).

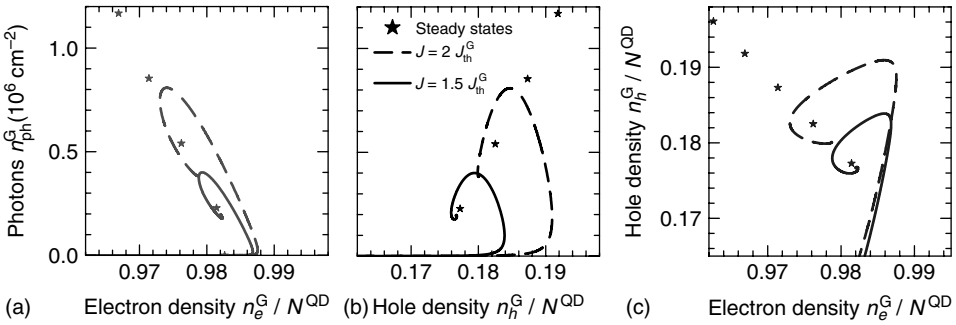

Figure 1.5 Turn-on trajectories for two different pump currents projected onto the (a) (n_e^G, n_{ph}^G)-plane, (b) (n_h^G, n_{ph}^G)-plane, and (c) (n_e^G, n_h^G)-plane; solid and dashed lines correspond to pump currents $J = 1.5J_{th}^G$ and $J = 2J_{th}^G$; stars represent the steady-state values for increasing pump currents. Parameters as in Table 1.1 but $B = 0.2$ nm^2 ps^{-1}, $\Delta E_e = 134$ meV and $\Delta E_h = 30$ meV.

1.3.1
Temperature Effects

So far, all simulations have been performed at a constant temperature of 300 K. In this section, the model is refined to account for carrier heating during laser operation. For the shift in the device temperature inside an electrically pumped optical amplifier (with identical active region as the laser diode considered here) Gomis-Bresco *et al.* [13] found values of $\Delta T = 60$ K at a pump current of $I =$ 150 mA, which is about 10 times $J_{\mathrm{th}}^{\mathrm{G}}$. Their measurement suggests a functional relationship of $\Delta T(J) \sim J^2$, which is adapted by implementing $\Delta T(w_e) \sim (w_e)^2$ (see Eq. (1.24)). It is noted that the steady-state relation $w_e^*(J)$ plotted for the discussed model in Figure 1.6f depends on the microscopic details of the scattering processes and is thus different for a QD laser with only one GS as in [26]. The physical reason for the carrier heating lies first in the facts that the carriers are injected into higher k-states during the electrical pumping. Second, the Auger scattering processes between QD and QW lead to scattering into high energy states inside the QW. Both effects change the carrier distribution and if the carriers in the reservoir do not have time to cool down to the lattice temperature, their temperature stays increased. (See [28] for a detailed kinetic modeling of the relaxation processes that allow to determine the carrier temperature from their distribution in *k*-space and [29] for microscopic calculations of the carrier heating in the low-density limit.) Consequently, the temperature entering the scattering rates is actually not the lattice temperature but the temperature of the carriers inside the QW that surrounds the QDs.

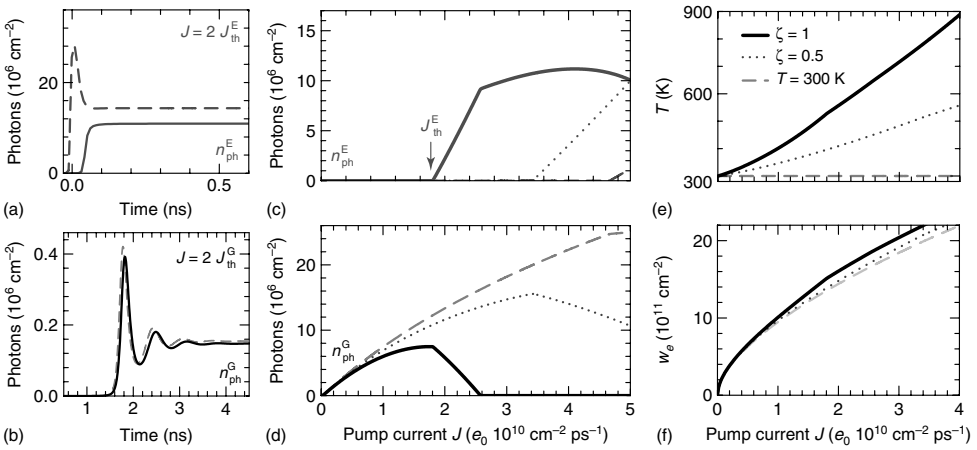

Figure 1.6 Simulated turn-on dynamics for (a) GS lasing ($J = 2J_{\mathrm{th}}^{\mathrm{G}}$) and (b) ES lasing ($J = 2J_{\mathrm{th}}^{\mathrm{E}}$). (c) and (d) show steady-state characteristics for ES and GS lasing, respectively. (e) and (f) show T and w_e as a function of the pump current J, respectively. In all plots, solid, dotted, and dashed lines represent simulations with increasing T according to Eq. (1.24) with $\zeta = 1$; $\zeta = 0.5$; and $\zeta = 0$. Parameters as in Table 1.1.

$$T = 300\ \mathrm{K} + \zeta \cdot \left(w_e/(w_{e|\mathrm{th}})\right)^2 \tag{1.24}$$

Note that an approach to directly implement $T(J)$, as in [30], suffers from the problem that a large signal modulation of the current leads to unphysical instantaneous switching in the temperature. An alternative approach is to determine the carrier heating from an additional rate equation for the energy density of the carriers in the reservoir [31].

Since the temperature enters the quasi-Fermi distribution that is assumed inside the QW, the microscopic scattering rates were calculated for several temperatures and implemented into the numeric simulation by approximated analytic expressions:

$$S_e^{\mathrm{in}}(T, w_e, w_h) = (1 + 0.22(T - 300\ \mathrm{K})/100\ \mathrm{K}) \cdot S_e^{\mathrm{in}}(300\ \mathrm{K}, w_e, w_h)$$
$$S_h^{\mathrm{in}}(T, w_e, w_h) = (1 + 0.26(T - 300\ \mathrm{K})/100\ \mathrm{K}) \cdot S_h^{\mathrm{in}}(300\ \mathrm{K}, w_e, w_h)$$

The out-scattering rates are related to the in-scattering rates by the detailed balance relations derived in Eqs. (1.13) and (1.14). Figure 1.6c,d shows the changes in the laser turn-on and steady-state dynamics if a dynamic temperature given by Eq. (1.24) is implemented for different constants ζ. The carrier temperature T and the carrier density in the reservoir w_e for the three cases are plotted in Figure 1.6e,f, respectively, as a function of J. Below the ES threshold current, the increasing temperature leads to a reduction in the differential efficiency of the GS steady-state characteristics as can be seen in Figure 1.6d. Furthermore, it reduces the ES threshold $J_{\mathrm{th}}^{\mathrm{E}}$, which results in two-state lasing at smaller pump currents (Figure 1.6c). In contrast to the case with constant T, the GS lasing is reduced as soon as the light is emitted from the ES. For high values of ζ, the GS lasing is completely suppressed. The turn-on dynamics of the ES is also affected by the high temperature (Figure 1.6a). Mainly due to the increased scattering rates at high T, the turn-on process becomes overdamped without a pronounced relaxation peak. At low currents close to the GS threshold $J_{\mathrm{th}}^{\mathrm{G}}$, the temperature does not change much and, thus, the turn-on process is also nearly unchanged (Figure 1.6b).

If these results are compared to two-state lasing experiments, a good agreement can be found. The suppression of the GS emission is indeed observed in experiments done by Wu *et al.* [32] on InP devices or by Ji *et al.* [30] on GaAs QD devices.

1.3.2 Impact of Energy Confinement

The energy diagram of the QD laser structure along the in-plane direction is shown in Figure 1.1. In principle, the sum $\Delta E_h + \Delta E_e$ can be determined from photoluminescence experiments that measure the energy of the GS emission of the QD ($h\nu_{\mathrm{GS}}$) and the wavelength of the QW emission. However, for the devices used here, there is a large uncertainty for the position of the QW band edge. Increasing the distance to the QD confined levels reduces the capture rates but does not have a large effect on the relaxation rates between the QD states. Simulations of the QD

laser with larger confinement energies ΔE_e and ΔE_h show two major changes in the dynamics. At first, the ratio between the threshold currents $J_{\mathrm{th}}^{\mathrm{E}}/J_{\mathrm{th}}^{\mathrm{G}}$ increases, as can be seen by comparing the steady-state characteristics shown in Figure 1.4b with the simulations for larger confinement energies in Figure 1.6c. The effect can be explained with the reduced capture rates into the ES, which inhibit an effective filling of the ES.

Another change in the dynamics that results from changes in the confinement energies is the reduced damping of the ROs. This can be seen if the GS turn-on in Figure 1.6b for higher $\Delta E_e(\Delta E_h) = 210(50)$ meV is compared to the turn-on with smaller $\Delta E_e(\Delta E_h) = 134(30)$ meV in Figure 1.4a. Similar to the case of a damped harmonic oscillator, the damping of the turn-on dynamics determines the response of the laser to a pump current that is modulated with a certain frequency and a small modulation amplitude. Modulation response curves obtained for different pump currents (close to the GS threshold) as a function of the modulating frequency are plotted in Figure 1.7a,c for the two different confinement energies discussed so far. Note that the parameter for the losses in the reservoir, B, is different in both cases to yield equal threshold currents of $J_{\mathrm{th}} = 3.4 \times 10^8 e_0$ cm^{-2} ps^{-1} and thus, according to Eq. (1.39), an RO frequency that is also observed in experiments (Figure 1.7b). The modulation response for the less damped case shown in Figure 1.7a shows a pronounced maximum at the frequency of the ROs, whereas it disappears for the strongly damped case in Figure 1.7c. The explanation for the impact of the confinement energies on the damping rate is given later on by using asymptotic methods in Section 1.5. There it is shown that the scattering rates, that is, the carrier lifetimes, determine the damping of the turn-on process, and increasing the lifetimes (decreasing the rates) of the smaller species (electrons) reduces the damping. The total lifetimes (including all capture and relaxation processes) of the GS levels are plotted in Figure 1.8a as a function of J for the two different cases discussed above. Obviously the lifetimes are decreased by decreasing ΔE_b but in

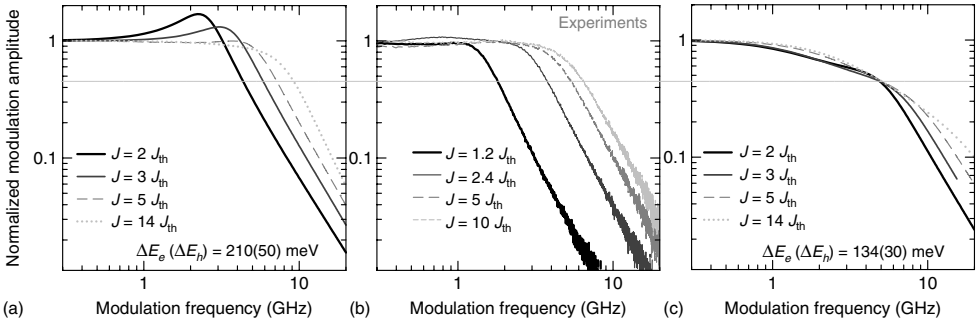

Figure 1.7 Small signal modulation response curves for different pump currents J simulated for confinement energies of (a) $\Delta E_e(\Delta E_h) = 210(50)$ meV ($B = 1.5\,\mathrm{nm}^2\ \mathrm{ps}^{-1}$) and (c) $\Delta E_e(\Delta E_h) = 134(30)$ meV ($B = 0.5\,\mathrm{nm}^2\ \mathrm{ps}^{-1}$). Other parameters as in Table 1.1. Measured curves taken from [6] are plotted in (b).

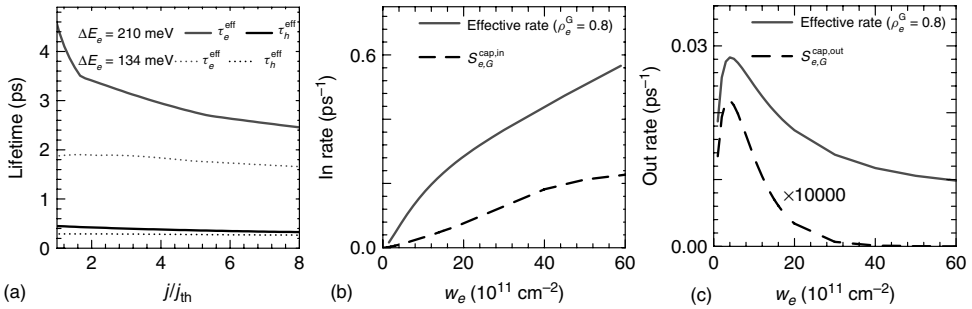

Figure 1.8 (a) Effective GS lifetimes τ_b^{eff} of electrons (gray) and holes (black) as a function of J for $\Delta E_e(\Delta E_h) = 210(50)$ meV (solid) and $\Delta E_e(\Delta E_h) = 134(30)$ meV (dotted). (b) and (c) show effective in- and out-scattering capture rates, respectively, resulting from adiabatic elimination of the ES variables according to Eq. (1.26).

both cases, the hole lifetimes are an order of magnitude smaller than those of the electrons.

1.3.3 Eliminating the Excited State Population Dynamics

One way to simplify the eight-variable rate equation system for the case where light is only emitted from the GS is to eliminate the ES carrier populations. This can be done by adiabatic elimination, which assumes a fast relaxation of the ES variables to their steady-state values and thus assumes $\dot{n}_b^{\mathrm{E}} = 0$. Using Eq. (1.15) gives

$$n_b^{\mathrm{E}}(w_e, w_h, n_b^{\mathrm{G}}) = \frac{2N^{\mathrm{QD}} S_{b,\mathrm{E}}^{\mathrm{cap,in}} + S_b^{\mathrm{rel,out}} n_b^{\mathrm{G}}}{S_{b,\mathrm{E}}^{\mathrm{cap,in}} + S_{b,\mathrm{E}}^{\mathrm{cap,out}} + (2N^{\mathrm{QD}})^{-1}\left[S_b^{\mathrm{rel,in}}(N^{\mathrm{QD}} - n_b^{\mathrm{G}}) + S_b^{\mathrm{rel,out}} n_b^{\mathrm{G}}\right]}. \tag{1.25}$$

Rewriting the remaining equations for w_b and n_b^{G} leads to

$$\dot{n}_b^{\mathrm{G}} = (N^{\mathrm{QD}} - n_b^{\mathrm{G}})\left[n_b^{\mathrm{E}} \frac{S_b^{\mathrm{rel,in}}}{2N^{\mathrm{QD}}} + S_{b,\mathrm{G}}^{\mathrm{cap,in}}\right] - R_{\mathrm{ind}}^{\mathrm{G}} - R_{\mathrm{sp}}^{\mathrm{G}} - n_b^{\mathrm{G}}\left[(2N^{\mathrm{QD}} - n_b^{\mathrm{E}}) \frac{S_b^{\mathrm{rel,out}}}{2N^{\mathrm{QD}}} + S_{b,\mathrm{G}}^{\mathrm{cap,out}}\right], \tag{1.26}$$

$$\dot{w}_b = \eta \frac{J(t)}{e_0} - N^{\mathrm{sum}} R_{b,\mathrm{G}}^{\mathrm{cap}} - \left[B w_e w_h + 2N^{\mathrm{sum}} R_{b,\mathrm{E}}^{\mathrm{cap}}\right], \tag{1.27}$$

Together with the unchanged equation for the photon density, Eq. (1.18), these equations resemble the five-variable case of a QD laser with one confined level if the terms in square brackets in Eq. (1.26) are interpreted as effective in- and out-scattering rates. They are, of course, different if compared to the values resulting from the pure GS scattering rates. The presence of the ES increases the scattering rates because of the possibility of in- or out-scattering via the relaxation cascade.

A comparison of the effective GS capture rates with the pure GS capture rates is shown in Figure 1.8b,c.

As already expected from the analytic expression in Eq. (1.26), the rates increase because of the relaxation rates that have to be added, but the overall nonlinear dependence on the QW carrier densities stays unchanged. The electron in-scattering rates increase by a factor of about 5, while a dramatic increase of 5×10^4 is observed for the electron out-scattering. Nevertheless the out-scattering rates stay an order of magnitude smaller than the in-scattering rates. For the holes the situation is different. The much higher GS out-scattering rate is comparable to the out-relaxation rate and for a large range of operation conditions the effective out-scattering rate is higher than the effective in-scattering rate. The resulting effective lifetimes of the GS levels for both carrier types, $\tau_b^{\text{eff}} = (S_b^{\text{in,eff}} + S_b^{\text{out,eff}})^{-1}$, are plotted in Figure 1.8a.

Another effect that results from the presence of an ES in the QD laser system is an increased loss rate in the equation for the QW carrier density (term in square brackets in Eq. (1.27)). This leads to higher threshold currents and to a speedup of the device.

To get a further insight into the correlations between the scattering rates and the turn-on dynamics, Section 1.5 discusses the analytic approximation for frequency and damping of the ROs of the QD laser. Before doing that, experimental results of QD lasers will be compared to numeric results obtained with the reduced five-variable rate-equation system.

1.4 Quantum Dot Switching Dynamics and Modulation Response

This section aims to discuss the modulation response and switching dynamics in comparison with experimental results [26]. Because the experimental results were obtained on a laser that showed only GS lasing, the reduced five-variable rate equation system of Section 1.3.3 is used for the simulations. As all quantities now refer to the GS, the superscript G is omitted in the following. The nonlinear rate equations (Eqs. (1.28)–(1.32)) describe the dynamics of the charge carrier densities in the QD GS, n_e and n_h, the carrier densities in the QW, w_e and w_h (e and h stand for electrons and holes, respectively), and the photon density n_{ph} of the GS transition.

$$\dot{n}_e = S_e^{\text{in}}(N^{\text{QD}} - n_e) - S_e^{\text{out}} n_e - WA(n_e + n_h - N^{\text{QD}})n_{\text{ph}} - R_{\text{sp}}, \tag{1.28}$$

$$\dot{n}_h = S_h^{\text{in}}(N^{\text{QD}} - n_h) - S_h^{\text{out}} n_h - WA(n_e + n_h - N^{\text{QD}})n_{\text{ph}} - R_{\text{sp}}, \tag{1.29}$$

$$\dot{w}_e = \eta\frac{J(t)}{e_0} - \frac{N^{\text{sum}}}{N^{\text{QD}}}\left[S_e^{\text{in}}(N^{\text{QD}} - n_e) - S_e^{\text{out}} n_e\right] - B(w_e)w_e w_h, \tag{1.30}$$

$$\dot{w}_h = \eta\frac{J(t)}{e_0} - \frac{N^{\text{sum}}}{N^{\text{QD}}}\left[S_h^{\text{in}}(N^{\text{QD}} - n_h) - S_h^{\text{out}} n_h\right] - B(w_e)w_e w_h, \tag{1.31}$$

$$\dot{n}_{\text{ph}} = -2\kappa n_{\text{ph}} + \Gamma WA(n_e + n_h - N^{\text{QD}})n_{\text{ph}} + \beta R_{\text{sp}}. \tag{1.32}$$

Here, the scattering rates S_b^{in} and S_b^{out} ($b = e, h$) used for the following simulations result from microscopic calculations that do not consider a second ES in the QDs. Their values as a function of the carrier densities w_b can be found in [8, 26]. Nevertheless, it is noted that similar results can been obtained with the full system discussed in Section 1.3.

1.4.1 Inhomogeneous Broadening

The spectral properties of the laser output are not addressed in the model, as the photon density is an average of all longitudinal modes inside the cavity. However, changes in the number of longitudinal modes are taken into account by changes in the active QD density N^{QD}, which basically changes the gain of the active medium. With a given QD size distribution p_i (where i is the index for a certain longitudinal mode frequency ν_i), the QD density participating in the emission at a given frequency ν_i is $N_i^{\text{QD}} = p_i N^{\text{sum}}$. Thus, the density of all active QDs is given by $N^{\text{QD}} = \sum_k p_k N^{\text{sum}}$ (the index k denotes the lasing longitudinal modes). The mode spacing inside the cavity ($L = 1$ mm) is $\Delta h\nu = 0.17$ meV($\Delta\lambda = 0.22$ nm), while the standard deviation of the QD size distribution [2] is about $\sigma_{\text{inh}} = 65$ meV $= 380\ \Delta h\nu$. Thus, 70% of all QDs are active ($N^{\text{QD}} = 0.7\ N^{\text{sum}}$) if the laser emits light at 380 longitudinal modes and only 3% ($N^{\text{QD}} = 0.03\ N^{\text{sum}}$) for a laser linewidth of 3.5 nm. On the basis of the experimental lasing spectra that show an increase in the lasing linewidth with increasing pump current (Figure 1.9), the pump-current-dependent spectral properties of the active QDs are

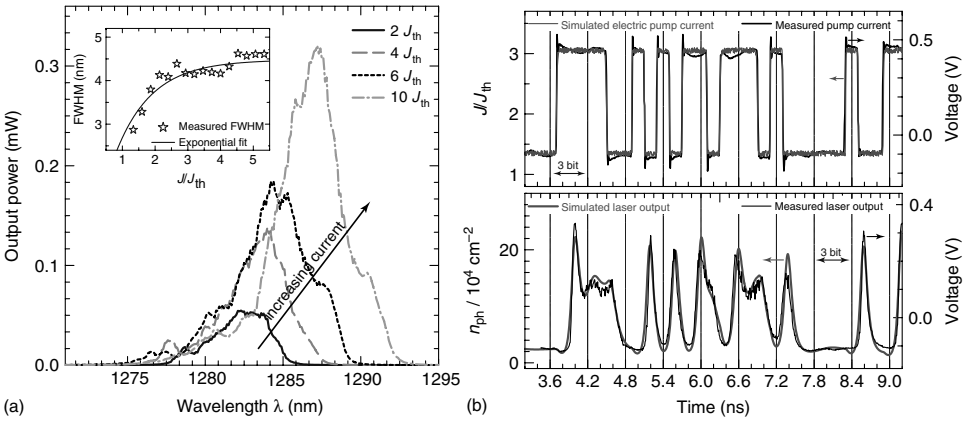

Figure 1.9 (a) Experimental lasing spectra for increasing pump currents illustrating the increasing number of longitudinal modes. Inset: Exponential fit (solid line) and FWHM of the measured spectra (stars), (b) Comparison between simulated (gray line) and measured data (black line) of electrical input signal (upper panel) and optical output (lower panel) versus time. Vertical lines show the separation into 3-bit sequences. (Reprinted from [26].)

taken into account and N^{QD} is implemented as a function of the QW carrier density [26] (Eq. (1.33)).

$$\frac{N^{QD}}{10^{-4}\ \mathrm{nm}^{-2}} = 0.75 - 0.74 \exp\left(-\frac{10^6}{1.75} w_e^2\right), \tag{1.33}$$

A more rigorous way to implement inhomogeneous broadening, which occurs in real devices because of fluctuations in QD size and material composition, and directly affects the energy levels, is accounted for by assuming a Gaussian size distribution around a central GS transition frequency ω_0 with standard deviation δ_ω. The spectral QD density is then given by $N(\omega) = \frac{N^{QD}}{\sqrt{2\pi}\delta_\omega} \exp\left[-\frac{(\omega-\omega_0)^2}{2\delta_\omega^2}\right]$ and the total QD density N^{QD} is approximated by a sum over a finite number of subensembles $N^{QD} = \sum_j N^j = \sum_j N(\omega_j)\Delta\omega$, where $\Delta\omega$ denotes the spectral width of the QD subgroups. Subsequently, a separate rate equation is used for each subensemble. For details, see, for example, [15, 33].

1.4.2 Temperature-Dependent Losses in the Reservoir

In addition to the temperature dependence of the in- and out-scattering rates discussed in Section 1.3.1, the carrier losses inside the reservoir will also be modeled as a function of T. The effect of these T-dependent losses will be most prominent for the large signal response of the laser while its effect on the turn-on dynamics and modulation response is small. The rate $R_{loss} = B w_e w_h$ that accounts for these losses is a sum of the spontaneous bimolecular band–band recombination and Auger-related losses inside the QW given by $B_A w_e w_e w_h$. The Auger coefficient B_A has been shown [34] to depend significantly on the temperature T, and is therefore implemented such that it leads to a doubling of the rate for a temperature change of 60 K (Eq. (1.24)) as found in [34]. Thus, $B_A = 305\ \mathrm{nm}^4\ \mathrm{ps}^{-1}\left(\frac{T}{300\ \mathrm{K}}\right)^4$ is used as given in [26]. Keep in mind that in this section a laser with only GS levels in the QDs is modeled. Within the extended model described in Section 1.3, the Auger scattering processes into the ES are already taken into account microscopically, which results in a different B_A for the remaining Auger processes within the QW. An alternative approach to model temperature characteristics is described in [35] by assuming nonradiative losses in the reservoir, which are modeled by capture processes from the reservoir to a midgap defect level.

1.4.3 Comparison to Experimental Results

The laser diode used for the experiments was a ridge waveguide InAs/InGaAs QD laser diode. The diode incorporates 15 stacks of QD layers having a DWELL structure [36]. The ridge is etched through the active layer to reduce current spreading [37] and to enhance wave guiding. The width of the ridge is 4 μm, while the length is 1 mm. To use the diode in high-frequency modulation schemes, top

p- and n-contacts in a ground-signal-ground (GSG) configuration, allowing the use of high-speed, low-loss probe heads, have been processed. The threshold current density $J_{\mathrm{th}}^{\mathrm{exp}}$ at room temperature is 380 A cm^{-2} with an emission wavelength close to 1.3 μm (Figure 1.9a). For pump currents, no ES lasing is found. Both facets of the laser are as cleaved. The diode is mounted on a copper heat sink and the light output is coupled to a standard single-mode fiber. A fiber-based isolator is used to prevent any feedback from influencing the laser diode. Eye diagrams have been obtained with an Agilent ParBert System, which creates an electrical pseudorandom binary sequence (PRBS) in a nonreturn to zero configuration. Here, a PRBS 5 (length: 2^5-1 bit) is used to make the results comparable to theoretical calculations.

Figure 1.9b shows the optical response of the laser to an electrical PRBS 5 signal switching between two levels (1.5 J_{th} and 3 J_{th}) of continuous wave (cw) operation. Simulated and experimentally determined input signals (electrical words) are shown in the upper panel of Figure 1.9b . Owing to the experimental setup (e.g., influence of cables and divider, oscilloscope noise), the measured pump-current signal (black line) is not as flat as the simulated time trace (gray line). Despite this small deviation, the measured optical response (black line, lower panel) matches the simulated laser output (gray line, lower panel) very well. Note that this agreement could only be achieved by including the dynamic parameters discussed in Section 1.4.1. For constant B, the relaxation peak that appears in the photon output after switching to higher currents (Figure 1.9b lower panel at $t = 4$ ns) could not be modeled because the long lifetime of the carriers in the QW inhibits fast changes in the QW carrier densities.

By superposing every 3-bit sequences of the laser output shown in Figure 1.9b, an eye diagram [38] is generated. These eye diagrams can be seen in Figure 1.10a,b, which shows measured and simulated eye patterns, respectively, for switching between two different current levels (left column: $J_{\mathrm{th}} \mapsto 3\,J_{\mathrm{th}}$ and right column: $4\,J_{\mathrm{th}} \mapsto 6\,J_{\mathrm{th}}$) and for three different pulse repetition frequencies (2.5, 5 and 10 GHz). Exact agreement in the shape (overshoots, trace, and extinction ratio) of the calculated and measured diagrams is found. Comparing the laser response for the different current levels it can be concluded that in order to improve the eye pattern diagrams, it is better to use higher current levels, as the relaxation peaks are thereby suppressed. The cutoff frequency of this QD laser – which is related to its RO frequency of 7 GHz – leads to a closing of the eyes already at 10 GHz. This can be improved by using higher pump currents; however, the modeling predicts that there is a trade-off since at the same time device heating results in further reduction of the RO frequency.

1.5 Asymptotic Analysis

As discussed in the previous sections, the solution to the QD laser equations exhibits different time scales that require accurate simulations. This section discusses an alternative to computationally expensive studies by using asymptotic methods. They

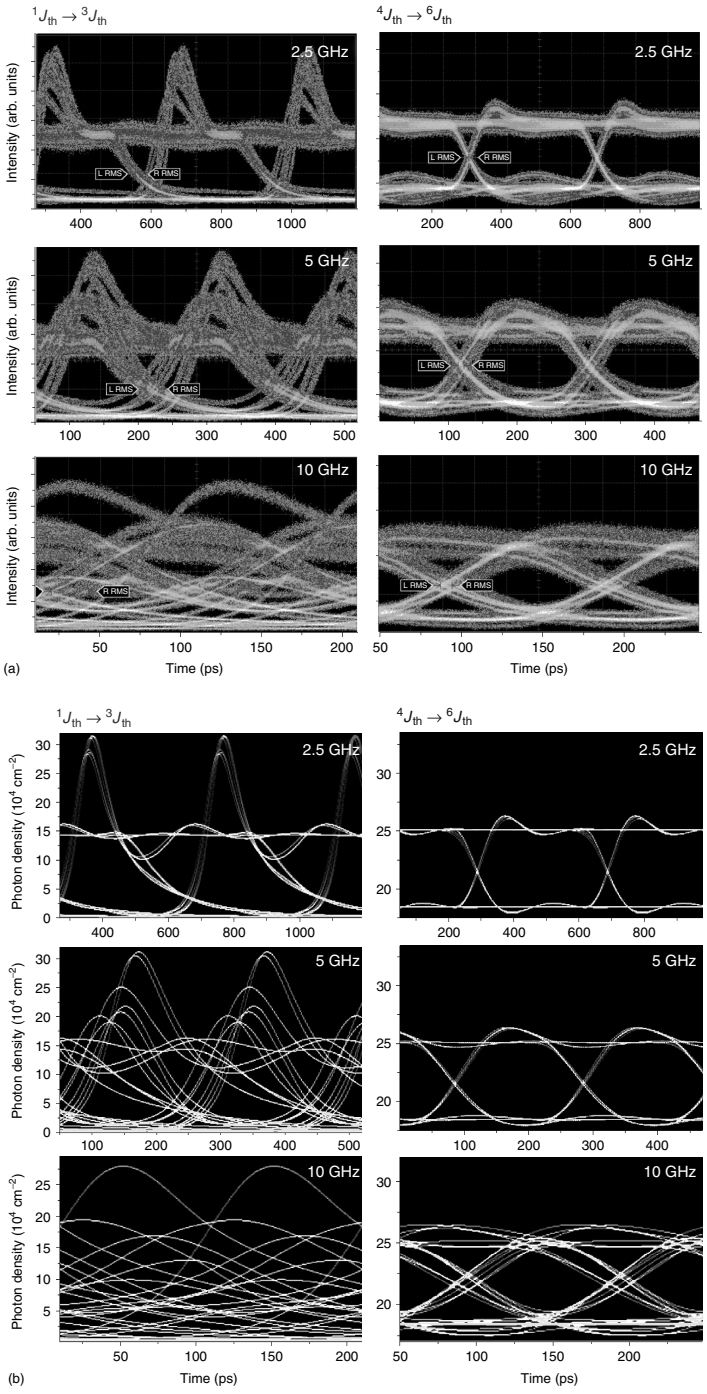

Figure 1.10 (a) Measured and (b) simulated eye diagrams for pump-current switching between $1J_{th}$ and $3J_{th}$ (left column) and between $4J_{th}$ and $6J_{th}$ (right column). Bit repetition frequency varies between 2.5 GHz (first line) and 10 GHz (third line). (Reprinted from [26].)

are motivated by the observation of quite different lifetimes between the carriers and the photons in the cavity ($\gamma = W/(2\kappa) \approx 7 \times 10^{-3}$). In order to simplify the rate equations, it is recalled that semiconductor lasers admit the properties of class B lasers. By applying approximation techniques appropriate for this class of lasers [39], it is possible to expand the full rate equation system in orders of $\sqrt{\gamma}$. The asymptotic techniques used for the analysis are described in detail in Chapter 6 [19], while the main results, that is, the analytic expressions for damping and frequency of the relaxation oscillations (ROs) of the laser, are discussed in the following. Note that the asymptotic results are valid only for scattering lifetimes that are on the order of several picoseconds or larger. For faster carriers the dynamics approaches the one of QW lasers and different scalings have to be used for the asymptotic analysis (see the limit large B in [46]).

The frequency ω_{RO} of the ROs can be obtained from the leading order problem of the expansion in powers of $\sqrt{\gamma}$ (see [40] for details) and is also valid far away from the fixed point. However, it is mathematically more convenient to determine the damping of the RO from the linearized problem including both $O(1)$ and $O(\sqrt{\gamma})$ terms. Thus, the damping rate of the ROs equals the real part of the eigenvalue λ of the characteristic polynomial of the linearized problem. To point out the effect of the scattering lifetimes τ_e and τ_h on the damping rate, the eigenvalues λ are computed as a function of the dimensionless parameter a_e and a_h defined as

$$a_e^{-1} = (S_e^{\mathrm{in}} + S_e^{\mathrm{out}})^{-1} \cdot \omega_{\mathrm{RO}} = \tau_e \cdot \omega_{\mathrm{RO}} \qquad \text{and} \qquad a_h^{-1} = \tau_h \cdot \omega_{\mathrm{RO}}. \tag{1.34}$$

The values of $\mathrm{Re}(\lambda)$ and $\mathrm{Im}(\lambda)$ are plotted in Figure 1.11a,b. It is striking that for constant and small a_e, the real part of λ first increases with a_h before it starts to decrease again. Thus, there is an optimal value for the carrier lifetimes if large damping is required. The parameter space for the carrier lifetimes explored

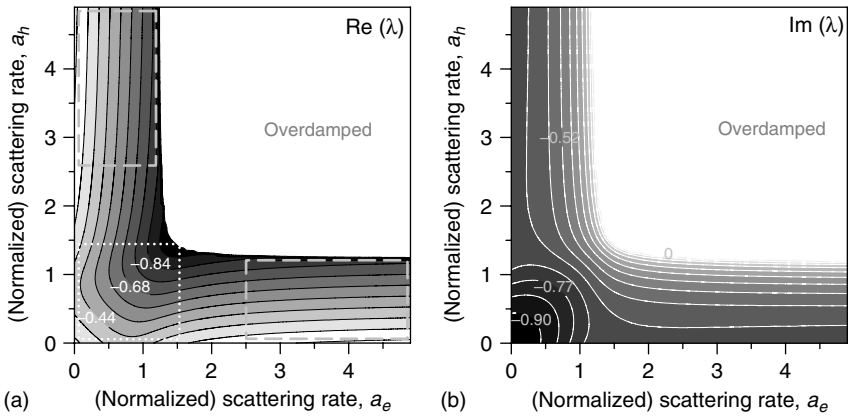

Figure 1.11 Contour plot of (a) real part and (b) imaginary part of the complex conjugate eigenvalue λ as a function of a_h and a_e. λ is determined from the Jacobian of the asymptotically expanded (up to $O(\sqrt{\gamma})$) and linearized laser problem. The white area marks the overdamped case with $\mathrm{Im}(\lambda) = 0$, while the squared, dotted, and rectangular dashed area mark "case S" and "case D", respectively.

in Figure 1.11 can be separated into three different areas. The ''overdamped case'' without ROs in the turn-on dynamics if both a parameters are large (small lifetimes); ''Case S'' having equal lifetimes for both species and ''Case D'' showing large timescale separation and, therefore, one large and one small parameter of a_e and a_h.

For the QD laser modeled in Section 1.4, the microscopic calculations yield fast hole scattering rates with lifetimes that are in the range of picoseconds. This leads to high values of a_h ($a_h > 5$), while the slower electrons with their small scattering rates are characterized by $a_e \approx 0$. Consequently, following the analytic approach for ''case D,'' the RO frequency and damping rate could be obtained, which are given by Lüdge *et al.* [40]

$$\omega_{RO}^{Da} = 2\pi f_{RO}^{Da} = \sqrt{An_{\mathrm{ph}}^{*} W 2\kappa}, \tag{1.35}$$

$$= \sqrt{\frac{\Gamma WAN^{\mathrm{QD}}}{N^{\mathrm{sum}}} J_{\mathrm{th}}^{\mathrm{G}} \left(\frac{J}{J_{\mathrm{th}}^{\mathrm{G}}} - 1 \right)} \tag{1.36}$$

$$\Gamma_{RO}^{Da} = \kappa An_{\mathrm{ph}}^{*} W\tau_h + \frac{1}{2\tau_e} + \frac{W}{2}(An_{\mathrm{ph}}^{*} + \frac{n_h^{*}}{N^{\mathrm{QD}}}) \tag{1.37}$$

$$\approx \frac{1}{2}(\omega_{RO}^{Da})^2 \left((2\kappa)^{-1} + \tau_h \right) + \frac{1}{2\tau_e} \tag{1.38}$$

where the superscript Da means case D with a_h large. The analytic solutions shown in Eqs. (1.35) and (1.37) for frequency and damping of the ROs have been compared to numerically obtained data in Figure 1.12b,c. Note the good agreement between the numeric values (symbols) and the analytic expressions (lines). The numeric values for ω_{RO} and Γ_{RO} have been obtained by fitting the function $n_{\mathrm{ph}}(t) \simeq C \sin(\omega_{\mathrm{RO}} t + \phi) \exp(-\Gamma_{\mathrm{RO}} t)$ to the turn-on transients. Equation (1.37) for the damping rate can be further simplified by omitting the smallest term (the one containing n_h^{*}), leading to Eq. (1.38). This reveals that the K-factor (ratio between damping rate and frequency squared [41, 42]) depends on three contributions. The smallest results from the scattering processes of the fast species (τ_h), the intermediate contribution is proportional to the cavity lifetime ($(2\kappa)^{-1}$), while the dominating effect scales with the scattering rates of the slow species. The RO frequency instead does not explicitly depend on the scattering rates, but is determined by $J_{\mathrm{th}}^{\mathrm{G}}$ and the differential gain ΓWA (Eq. (1.36) obtained by inserting the steady-state relation n_{ph}^{*} from Eq. (1.20)).

A different scaling is found for ''case S'' (see [40]) with small scattering rates for both carrier types (this can be achieved by changing the band structure and increasing the hole confinement energy).

$$\omega_{\mathrm{RO}}^{S} = \sqrt{2An_{\mathrm{ph}}^{*} W 2\kappa} \tag{1.39}$$

$$\Gamma_{\mathrm{RO}}^{S} = \frac{W}{2}[2An_{\mathrm{ph}}^{*} + 1] + \frac{\kappa}{\Gamma AN^{\mathrm{QD}}} + \frac{1}{4\tau_e} + \frac{1}{4\tau_h} \tag{1.40}$$

$$\approx \frac{1}{2}(\omega_{\mathrm{RO}}^{S})^2 (2\kappa)^{-1} + \frac{1}{4\tau_e} + \frac{1}{4\tau_h}. \tag{1.41}$$

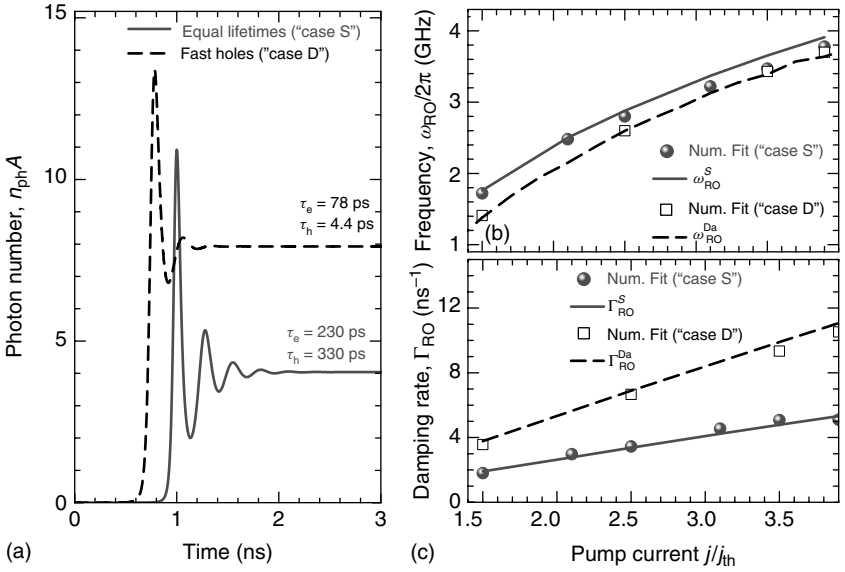

Figure 1.12 (a) Turn-on dynamics of the QD laser for "case S" (similar lifetimes) (gray solid) and "case D" (different lifetimes) (black dashed) at $J = 3.7J_{th}$. (b) and (c) show comparisons between numerically fitted data (symbols) and analytical data obtained from Eqs. (1.35)–(1.40) (lines) for the RO frequency and RO damping rate, respectively. ($n_{ph}(t) \simeq C\sin(\omega_{RO}t + \phi)\exp(-\Gamma_{RO}t)$ is used to extract ω_{RO} and Γ_{RO} from the numerical simulation of $n_{ph}(t)$).

For this "case S," the expression of the RO frequency in Eq. (1.39) is the same as the one for the conventional semiconductor laser [39]. However, the expression of the damping rate is different. It contains the familiar term $\frac{W}{2}\left[2An_{ph}^{*}+1\right]$ that is found for the damping rate of QW lasers [19], but as already known from "case D" the dominating contribution stems from the scattering rates between QD and the reservoir.

By changing the confinement energy in the numeric calculations of the scattering rates it is possible to obtain small scattering rates and thus a "case S" like behaviour of the QD laser. The results of this simulation are plotted in Figure 1.12a showing weakly damped ROs. The analytic expressions accurately predict this behavior (see lines in Figure 1.12b,c), which makes them a powerful analytical tool for designing QD laser devices with optimal operation conditions.

1.5.1
Consequences of Optimizing Device Performance

The analytical expressions for the RO frequency and RO damping rate for the different parameter ranges show that the RO frequency ω_{RO} does not explicitly depend on the carrier–carrier scattering between QW and QD. It strongly depends on the cavity lifetime $(2\kappa)^{-1}$ and radiative recombination lifetime W^{-1} and on the

threshold current of the QD laser, which are determined by the gain, the ratio between in- and out-scattering rates, and the losses in the QW.

The damping rate Γ_{RO}, instead, is crucially affected by the carrier–carrier scattering rates. For equal lifetimes of electrons and holes, the damping increases with decreasing lifetimes τ_e and τ_h. If both carrier types have different lifetimes, only the slowest species (for the chosen QD–QW system, these are the electrons) determines the damping rate, whereas the effect of the fast species is negligible.

In the next section, numeric simulations of QD lasers with doped carrier reservoir are discussed. Owing to the density-dependent Coulomb scattering rates, the doping modifies the carrier lifetimes in a controlled way and thus it is a good tool on the one hand for testing the analytics and on the other hand to optimize the device performance.

1.6 QD Laser with Doped Carrier Reservoir

A doped QW can be implemented by choosing different initial conditions for electron and hole densities in the QW. Without doping, the following initial conditions have been used, that is, $n_e^0 = 0$, $n_h^0 = 0$, $w_e^0 = 10^{-2} D_e kT$, and $w_h^0 = 10^{-2} D_e kT$. Note that charge conservation is contained in the five-variable rate equation system Eqs. (1.28)–(1.32), thus leading to only four independent dynamic variables that are related by

$$N^{\mathrm{sum}}(\dot{n}_e - \dot{n}_h) - N^{\mathrm{QD}}(\dot{w}_h - \dot{w}_e) = 0 \tag{1.42}$$

which can be integrated giving

$$N^{\mathrm{sum}}(n_e - n_h) - N^{\mathrm{QD}}(w_h - w_e) = N^{\mathrm{QD}}(w_e^0 - w_h^0). \tag{1.43}$$

By increasing w_e^0 or w_h^0 and keeping the other at the small value of $10^{-2} D_e kT$, it is possible to model n- or p-doping, respectively. Because the rate equation system treats 2D densities, the doping concentrations $n \approx w_e^0$ and $p \approx w_h^0$ are also given per area. To compare this to 3D doping densities, the areal densities have to be divided by the QW height, which is $h = 4\,\mathrm{nm}$. Thus, $n = 2 \times 10^{11}\mathrm{cm}^{-2}$ corresponds to $n_{3D} = 5 \times 10^{17}\mathrm{cm}^{-3}$. Figure 1.13c,d shows that changes in initial conditions drastically modify the QD laser turn-on dynamics. For n-doping, the damping of the ROs is increased, whereas the damping is drastically reduced if p-doping is introduced. This behavior can be understood by discussing the steady-state values for the QW carrier densities w_b.

N-doping increases the QW electron density, which then leads to higher in-scattering rates S_e^{in} (Figure 1.3) and, therefore, to higher carrier densities n_e^*. On the contrary, p-doping leads to a higher QW hole concentration and thus to higher occupation of the QD hole levels. Note, however, that the increased QW hole density for p-doped samples also has an effect on the out-scattering rate, as this contains a factor that exponentially decreases with w_e through the detailed balance relation (Eq. (1.13)). The scattering time τ_h for holes decreases with increasing p-doping,

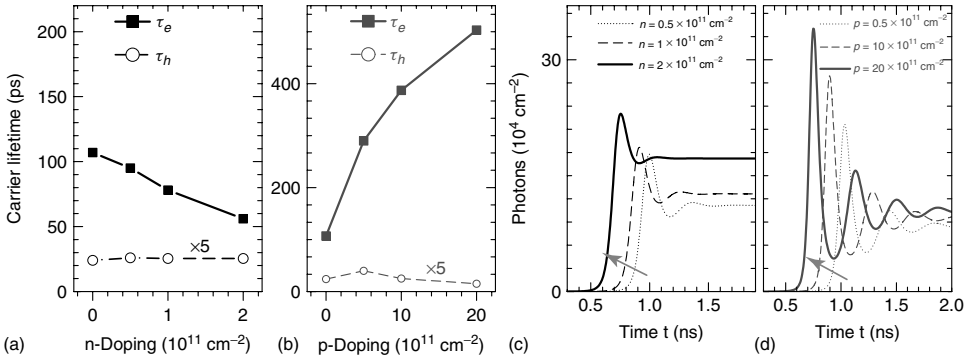

Figure 1.13 (a,b): Carrier lifetimes as a function of (a) n-doping and (b) p-doping density. (b,c): Time series of the photon density during laser turn-on for (c) different n-doping density and (d) different p-doping density. Dotted, dashed, and solid lines correspond to doping of 0.1, 0.2, and 0.4 times the degeneracy concentration $D_{e/h}kT$, respectively. ($D_e kT = 4.7 \times 10^{11}$ cm^{-2} and $D_h kT = 48 \times 10^{11}$ cm^{-2}). Parameters as in Table 1.1; pump current is $J = 2.5 J_{\text{th}}$.

while the scattering time for electrons increases as plotted in Figure 1.13b. The ratio between the timescales of both carriers decreases from $\tau_h/\tau_e = 5/100$ for the undoped case to a value of $\tau_h/\tau_e = 3/500$ for a p-doping of $p = 20 \times 10^{11}$ cm^{-2}. Using the analytic expression Eq. (1.37) for the damping rate explains that the lower damping results from the longer lifetime of the small species, whereas the changes in the hole lifetime only marginally affect the damping rate.

Figure 1.14a shows the steady-state characteristics of the QD laser projected onto the (n_h, n_e)-phase space for two different n-doping densities (squares and triangles) and two different p-doping densities (open circles and stars). Figure 1.14b,c shows close-ups for very high p-doping. Going from high p-doping to n-doping, the steady states n_e^* and n_h^* move up along an approximately straight line in (n_h, n_e)-phase space that is given by Eq. (1.23), while the turn-on dynamics becomes more strongly damped and synchronized between electrons and holes. This is different from changing the steady-state values by varying the confinement energy as the increased steady-state values n_e^* (induced by increasing ΔE_e) lead to a desynchronization (separation of timescales) of electrons and holes.

Comparison with Analytic Results

The analytical approximations of Section 1.5 and the obtained predictions about changes in the laser turn-on dynamics are in good agreement with the numerical simulations of a laser with different doping densities discussed in the last section. The increasing n-doping concentration in a QD laser with timescale separation of the carriers (''case D'' in Section 1.5) leads to a decrease in the electron lifetime, which was at the same time accompanied by an increased damping. With the analytic formula given in Eq. (1.37), the increased damping can be explained with the decreased lifetime ($S_e^{\text{in}} + S_e^{\text{out}} = \tau_e^{-1}$ increases). On the other hand, p-doping

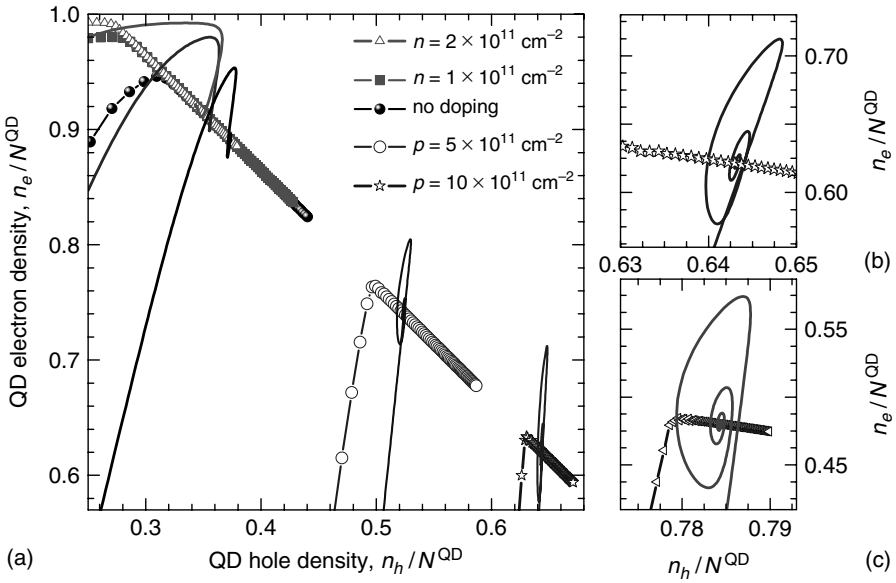

Figure 1.14 Effect of QW doping: steady-state characteristic for a range $J = 0$ to $J/e_0 = 2 \times 10^9$ cm^{-2} (symbols) and turn-on trajectories for $J = 2.5 J_{th}$ (lines) projected onto the (n_h, n_e)-phase space (a) squares, triangles, circles, and stars are doping densities of $n = 1 \times 10^{11}$ cm^{-2}, $n = 2 \times 10^{11}$ cm^{-2}, $p = 5 \times 10^{11}$ cm^{-2}, and $p = 10 \times 10^{11}$ cm^{-2}, respectively; (b) and (c): close-up of (a) for $p = 10 \times 10^{11}$ cm^{-2} and $p = 20 \times 10^{11}$ cm^{-2}, respectively. Parameters as in Table 1.1. (Reprinted from [8].)

of the same device did not yield a higher RO damping. The reason for this counterintuitive result is the separation of timescales of electron and hole lifetimes (which is the case for material with large differences in the effective masses of electrons and holes). The slowest species determines the dynamics and, thus, manipulating its lifetime has a drastic effect on the laser dynamics (Eq. (1.37)). Instead, manipulating the lifetime of the fast species has only a minor effect. The reduced damping for p-doping concentration is based on a reduction of the electron lifetimes, which has its physical origin in the increased rate for mixed electron–hole Coulomb scattering processes because of the excess holes in the reservoir. It confirms that p-doping is beneficial for the modulation response of QD lasers [43]. If a high RO damping rate is a desired property of QD lasers, n-doping should be helpful.

1.7 Model Reduction

One way to simplify the discussed QD laser model is to neglect the density dependence of the scattering rates and to use constant carrier lifetimes; see, for example, [27, 33, 35]. If these lifetimes are chosen properly, they can lead to decent results at a certain point of operation. Nevertheless, the uncertainty in the choice

of proper simulation parameters, which is necessary for those models, will lead to a large uncertainty regarding the results. Moreover, effects such as doping or the effect of changing the QD size cannot be studied. There are also approaches that take into account a phenomenological density dependence of the carrier lifetimes; see, for example, [44], but again the problem of choosing the correct parameters remains.

A simpler three-variable rate equation model was formulated by O'Brien *et al.* [45] and is widely used for QD laser modeling (see [46] for detailed analytic discussions of this model). This model does not distinguish between electrons and holes; it assumes the same dynamics for both species, and it uses in-scattering rates into the QDs that linearly increase with the reservoir carrier density, while the out-scattering rates are constant. Following the analytic results of Section 1.5, a reduction in the full microscopic five-variable model to a model that only assumes one carrier type is possible, but two cases have to be distinguished. If electrons and holes relax on a similar timescale (''case S''), the mean value of electron and hole rates needs to be included; however, for timescale separation between the lifetimes of the species (''case D''), the scattering rate of the slow species will be the important one that determines the dynamics. If this is kept in mind, the (linearly fitted) microscopic in-scattering rates can be used as input parameters for the three-variable rate equation system. Nevertheless, it has to be noted that these parameters need to be adjusted if large variations of the pump current or different doping densities are modeled.

1.8
Comparison to Quantum Well Lasers

If a QD laser model is compared to a QW laser model [47, 48], one striking difference is that the current is not injected directly into the active region, and an additional reservoir has to be included. The relatively slow scattering processes from the carrier reservoir into the QD levels are responsible for the high damping of the turn-on process (Section 1.5) and thus also for the flat modulation response curve of QD lasers if compared to the pronounced peak found for QW lasers. In the limit of large and equal scattering rates for electrons and holes, the QD laser model can be reduced to a QW laser model as shown in [46]. However, the modulation bandwidth (and the cutoff frequency) of QD lasers is also much smaller because of the smaller RO frequency. The reason for this lies in the fact that the threshold currents needed to invert the localized two-level system is much smaller than the current needed to invert a 2D electron gas.

If complex integrated structures, for example, QD lasers subjected to optical feedback [18, 49] or lasers with saturable absorber are discussed (see Chapter 7 [50] and Chapter 8 [51]), the high damping of the turn-on dynamics of the QD laser is one crucial parameter when discussing differences with respect to QW lasers. Another parameter that differs between QD and QW laser devices is the phase–amplitude coupling (linewidth enhancement factor). It comes into play as soon as the phase

of the electric field is important, for example, when modeling feedback problems (see Chapter 6 [19]). For a discrete two-level system, the α-factor is zero because of the symmetric gain spectrum. For an inhomogeneously broadened ensemble of QDs inside the QD laser, α still remains small [52] and leads, for example, to a smaller chirp and higher feedback sensitivity of QD lasers (see [18] for a comparison of both laser models with feedback).

1.9 Summary

This chapter reviewed a microscopic rate equation approach that can be used to model the dynamic response of electrically pumped edge emitting QD lasers. Different levels of complexity have been explored. A detailed discussion of the Coulomb scattering rates between localized QD levels and the 2D carrier reservoir in the surrounding QW has underlined the importance of these nonlinear Auger rates for a quantitative modeling of the QD laser device. Two-state lasing properties as well as the effect of additional confined levels on the GS lasing properties have been analyzed. It was shown that temperature, band structure, as well as doping of the carrier reservoir can significantly alter the laser dynamics. Nevertheless, all of these effects can be traced back to the values of the carrier–carrier scattering rates and their nonlinear dependence on the carrier densities in the reservoir. Furthermore, asymptotic analysis has allowed analytic insights into the relations between frequency and damping of the turn-on dynamics and the carrier lifetimes that finally permitted to predict the dynamics of the laser without tedious numeric simulations, and provide insight into the governing physical mechanism.

Acknowledgment

I am grateful to Prof. Eckehard Schöll for giving me the opportunity to do research about QD lasers within his group. My thanks also go to Niels Majer for his excellent work in calculating the microscopic scattering rates and to Thomas Erneux for the great collaboration on the asymptotic analysis of the QD laser model. This work was supported by DFG in the framework of Sfb 787.

References

1. Bimberg, D., Fiol, G., Kuntz, M., Meuer, C., Lämmlin, M., Ledentsov, N.N., and Kovsh, A.R. (2006) High speed nanophotonic devices based on quantum dots. *Phys. Stat. Sol. A*, **203** (14), 3523–3532. DOI: 10.1002/pssa.200622488.
2. Bimberg, D., Grundmann, M., and Ledentsov, N.N. (1999) *Quantum Dot Heterostructures*, John Wiley & Sons, Inc, New York.
3. Rafailov, E.U., Cataluna, M.A., and Avrutin, E.A. (2011) *Ultrafast Lasers Based on Quantum Dot Structures*, Wiley-VCH Verlag GmbH, Weinheim.
4. Malić, E., Ahn, K.J., Bormann, M.J.P., Hövel, P., Schöll, E., Knorr, A.,

Kuntz, M., and Bimberg, D. (2006) Theory of relaxation oscillations in semiconductor quantum dot lasers. *Appl. Phys. Lett.*, **89**, 101107. DOI: 10.1063/1.2346224.

5. Malić, E., Bormann, M.J.P., Hövel, P., Kuntz, M., Bimberg, D., Knorr, A., and Schöll, E. (2007) Coulomb damped relaxation oscillations in semiconductor quantum dot lasers. *IEEE J. Sel. Top. Quantum Electron.*, **13** (5), 1242–1248. DOI: 10.119/jqstqe.2007.905148.
6. Lüdge, K., Bormann, M.J.P., Malić, E., Hövel, P., Kuntz, M., Bimberg, D., Knorr, A., and Schöll, E. (2008) Turn-on dynamics and modulation response in semiconductor quantum dot lasers. *Phys. Rev. B*, **78** (3), 035316. DOI: 10.1103/physrevb.78.035316.
7. Lüdge, K. and Schöll, E. (2009) Quantum-dot lasers - desynchronized nonlinear dynamics of electrons and holes. *IEEE J. Quantum Electron.*, **45** (11), 1396–1403.
8. Lüdge, K. and Schöll, E. (2010) Nonlinear dynamics of doped semiconductor quantum dot lasers. *Eur. Phys. J. D*, **58**, 167–174. DOI: 10.1140/epjd/e2010-00041-8.
9. Chow, W.W. and Koch, S.W. (1999) *Semiconductor-Laser Fundamentals*, Springer.
10. Su, Y., Carmele, A., Richter, M., Lüdge, K., Schöll, E., Bimberg, D., and Knorr, A. (2011) Theory of single quantum dot lasers: Pauli-blocking enhanced anti-bunching. *Semicond. Sci. Technol.*, **26**, 014015.
11. Chow, W.W. and Koch, S.W. (2005) Theory of semiconductor quantum-dot laser dynamics. *IEEE J. Quantum Electron.*, **41**, 495–505. DOI: 10.1109/jqe.2005.843948.
12. Lingnau, B., Lüdge, K., Schöll, E., and Chow, W.W. (2010) Many-body and nonequilibrium effects on relaxation oscillations in a quantum-dot microcavity laser. *Appl. Phys. Lett.*, **97** (11), 111102. DOI: 10.1063/1.3488004.
13. Gomis-Bresco, J., Dommers, S., Temnov, V.V., Woggon, U., Martinez-Pastor, J., Lämmlin, M., and Bimberg, D. (2009) InGaAs quantum dots coupled to a reservoir of nonequilibrium free carriers. *IEEE J. Quantum Electron.*, **45** (9), 1121–1128.
14. Wegert, M., Majer, N., Lüdge, K., Dommers-Völkel, S., Gomis-Bresco, J., Knorr, A., Woggon, U., and Schöll, E. (2011) Nonlinear gain dynamics of quantum dot optical amplifiers. *Semicond. Sci. Technol.*, **26**, 014008.
15. Majer, N., Lüdge, K., and Schöll, E. (2010) Cascading enables ultrafast gain recovery dynamics of quantum dot semiconductor optical amplifiers. *Phys. Rev. B*, **82**, 235301.
16. Majer, N., Lüdge, K., Gomis-Bresco, J., Dommers-Völkel, S., Woggon, U., and Schöll, E. (2011) Impact of carrier-carrier scattering and carrier heating on pulse train dynamics of quantum dot semiconductor optical amplifiers. *Appl. Phys. Lett.*, **99**, 131102, doi:10.1063/1.3643048.
17. Sciamanna, M. Mode competition driving laser nonlinear dynamics, Chapter 3 this book.
18. Otto, C., Lüdge, K., and Schöll, E. (2010) Modeling quantum dot lasers with optical feedback: sensitivity of bifurcation scenarios. *Phys. Stat. Sol. B*, **247** (4), 829. DOI: 10.1002/pssb.200945434.
19. Otto, C. Lüdge, K., Viktorov, E.A., and Erneux, T. (2011) Quantum dot laser tolerance to optical feedback, Chapter 6 this book.
20. Lorke, M., Nielsen, T.R., Seebeck, J., Gartner, P., and Jahnke, F. (2006) Influence of carrier-carrier and carrier-phonon correlations on optical absorption and gain in quantum-dot systems. *Phys. Rev. B*, **73**, 085324. DOI: 10.1103/physrevb.73.085324.
21. Nielsen, T.R., Gartner, P., and Jahnke, F. (2004) Many-body theory of carrier capture and relaxation in semiconductor quantum-dot lasers. *Phys. Rev. B*, **69**, 235314.
22. Nilsson, H.H., Zhang, J.Z., and Galbraith, I. (2005) Homogeneous broadening in quantum dots due to auger scattering with wetting layer carriers. *Phys. Rev. B*, **72** (20), 205331. DOI: 10.1103/physrevb.72.205331.
23. Schöll, E., Amann, A., Rudolf, M., and Unkelbach, J. (2002) Transverse

spatio-temporal instabilities in the double barrier resonant tunneling diode. *Physica B*, **314**, 113.

24. Schöll, E. (1987) *Nonequilibrium Phase Transitions in Semiconductors*, Springer, Berlin.
25. Lasher, G. and Stern, F. (1964) Spontaneous and stimulated recombination radiation in semiconductors. *Phys. Rev.*, **133** (2A), A553.
26. Lüdge, K., Aust, R., Fiol, G., Stubenrauch, M., Arsenijević, D., Bimberg, D., and Schöll, E. (2010) Large signal response of semiconductor quantum-dot lasers. *IEEE J. Quantum Electron.*, **46** (12), 1755–1762. DOI: 10.1109/jqe.2010.2066959.
27. Markus, A., Chen, J.X., Paranthoen, C., Fiore, A., Platz, C., and Gauthier-Lafaye, O. (2003) Simultaneous two-state lasing in quantum-dot lasers. *Appl. Phys. Lett.*, **82** (12), 1818.
28. Lingnau, B., Lüdge, K., Schöll, E., and Chow, W.W. (2010) in *Dynamic Many-Body and Nonequilibrium Effects in a Quantum Dot Microcavity Laser*, Proceedings of SPIE, vol. 7720, (eds K. Panajotov, M. Sciamanna, A.A. Valle, and R. Michalzik), pp. 77201F-77201F-11. DOI: 10.1117/12.854671.
29. Wolters, J., Dachner, M.R., Malić, E., Richter, M., Woggon, U., and Knorr, A. (2009) Carrier heating in light emitting quantum-dot heterostructures at low injection currents. *Phys. Rev. B*, **80**, 245401.
30. Ji, H.M., Yang, T., Cao, Y.L., Xu, P.F., and Gu, Y.X. (2010) Self-heating effect on the two-state lasing behaviors in 1.3-μm InAs-GaAs quantum-dot lasers. *Jpn. J. Appl. Phys.*, **49**, 072103.
31. Uskov, A.V., Meuer, C., Schmeckebier, H., and Bimberg, D. (2011) Auger capture induced carrier heating in quantum dot lasers and amplifiers. *Appl. Phys. Express*, **4** (2), 022202. DOI: 10.1143/apex.4.022202.
32. Wu, D.C., Su, L.C., Lin, C.Y., Mao, M.H., Wang, J.S., Lin, G., and Chi, J.Y. (2009) Experiments and simulation of spectrally-resolved static and dynamic properties in quantum dot two-state lasing. *Jpn. J. Appl. Phys.*, **48**, 032101.
33. Gioannini, M., Sevega, A., and Montrosset, I. (2006) Simulations of differential gain and linewidth enhancement factor of quantum dot semiconductor lasers. *Opt. Quantum Electron.*, **38**, 381–394. DOI: 10.1007/s11082-006-0038-1.
34. Pikal, J.M., Menoni, C.S., Thiagarajan, P., Robinson, G.Y., and Temkin, H. (2000) Temperature dependence of intrinsic recombination coefficients in 1.3 μm InAsP/InP quantum-well semiconductor lasers. *Appl. Phys. Lett.*, **76** (19), 2659–2661.
35. Rossetti, M., Fiore, A., Sek, G., Zinoni, C., and Li, L. (2009) Modeling the temperature characteristics of InAs/GaAs quantum dot lasers. *J. Appl. Phys.*, **106** (2), 023105. DOI: 10.1063/1.3176499.
36. Kovsh, A.R., Maleev, N.A., Zhukov, A.E., Mikhrin, S.S., Vasil'ev, A.V., Semenova, A., Shernyakov, Y.M., Maximov, M.V., Livshits, D.A., Ustinov, V.M., Ledentsov, N.N., Bimberg, D., and Alferov, Z.I. (2003) InAs/InGaAs/GaAs quantum dot lasers of 1.3 μm range with enhanced optical gain. *J. Crystal Growth*, **251**, 729–736.
37. Ouyang, D., Ledentsov, N.N., Bimberg, D., Kovsh, A.R., Zhukov, A.E., Mikhrin, S.S., and Ustinov, V.M. (2003) High performance narrow stripe quantum-dot lasers with etched waveguide. *Semicond. Sci. Technol.*, **18**, L53–L54.
38. Derickson, D. and Müller, M. (2007) *Digital Communications Test and Measurement: High-Speed Physical Layer Characterization*, Prentice Hall Press, Upper Saddle River, NJ.
39. Erneux, T. and Glorieux, P. (2010) *Laser Dynamics*, Cambridge University Press, UK.
40. Lüdge, K., Schöll, E., Viktorov, E.A., and Erneux, T. (2011) Analytic approach to modulation properties of quantum dot lasers. *J. Appl. Phys.* **109** (9), 103112.
41. Olshansky, R., Hill, P., Lanzisera, V., and Powazinik, W. (1987) Frequency response of 1.3 μm InGaAsP high speed semiconductor lasers. *IEEE J. Quantum Electron.*, **23** (9), 1410–1418.
42. Klotzkin, D. and Bhattacharya, P. (1999) Temperature dependence of dynamic and dc characteristics of quantum-well

and quantum-dot lasers: a comparative study. *J. Lightwave Technol.*, **17** (9), 1634.

43. Shchekin, O.B. and Deppe, D.G. (2002) The role of p-type doping and the density of states on the modulation response of quantum dot lasers. *Appl. Phys. Lett.*, **80** (15), 2758–2760. DOI: 10.1063/1.1469212.
44. Veselinov, K., Grillot, F., Cornet, C., Even, J., Bekiarski, A., Gioannini, M., and Loualiche, S. (2007) Analysis of the double laser emission occurring in 1.55 μm InAs–InP (113)B quantum-dot lasers. *IEEE J. Quantum Electron.*, **43** (9), 810–816. DOI: 10.1109/jqe.2007.902386.
45. O'Brien, D., Hegarty, S.P., Huyet, G., and Uskov, A.V. (2004) Sensitivity of quantum-dot semiconductor lasers to optical feedback. *Opt. Lett.*, **29** (10), 1072–1074.
46. Erneux, T., Viktorov, E.A., and Mandel, P. (2007) Time scales and relaxation dynamics in quantum-dot lasers. *Phys. Rev. A*, **76**, 023819. DOI: 10.1103/physreva.76.023819.
47. Schöll, E., Bimberg, D., Schumacher, H., and Landsberg, P.T. (1984) Kinetics of picosecond pulse generation in semiconductor lasers with bimolecular recombination at high current injection. *IEEE J. Quantum Electron.*, **20**, 394.
48. Schöll, E. (1988) Dynamic theory of picosecond optical pulse shaping by gain-switched semiconductor laser amplifiers. *IEEE J. Quantum Electron.*, **24** (2), 435–442.
49. Otto, C., Globisch, B., Lüdge, K., Schöll, E., and Erneux, T. (2012) Complex dynamics of semiconductor quantum dot lasers subject to delayed optical feedback. *Int. J. Bifurcat. Chaos* (accepted publication).
50. Krauskopf, B. and Walker, J.J. (2011) Bifurcation study of a semiconductor laser with saturable absorber and delayed optical feedback, Chapter 7 this book.
51. Vladimirov, G., Rachinskii, D., and Wolfrum, (2011) Modeling of passively mode-locked semiconductor lasers, Chapter 8 this book.
52. Kim, J. and Chuang, S.L. (2006) Theoretical and experimental study of optical gain, refractive index change, and linewidth enhancement factor of p-doped quantum-dot lasers. *IEEE J. Quantum Electron.*, **42** (9), 942–952. DOI: 10.1109/jqe.2006.880380.